Università degli Studi di Palermo

Dottorato di Ricerca in Scienze Chimiche XXIV Ciclo

Studio di materiali avanzati per celle a combustibile ad ossidi solidi: influenza dei droganti e delle tecniche di sintesi sulle proprietà di anodi ed elettroliti

Chiara Aliotta

Tutor:
Prof. Antonino Martorana
Co-tutor:
Dr. Francesca Deganello
Coordinatore:
Prof. Paolo Lo Meo

Università degli Studi di Palermo

Dottorato di Ricerca in Scienze Chimiche XXIV Ciclo

Studio di materiali avanzati per celle a combustibile ad ossidi solidi: influenza dei droganti e delle tecniche di sintesi sulle proprietà di anodi ed elettroliti

Chiara Aliotta

Tutor:
Prof. Antonino Martorana

Co-tutor:
Dr. Francesca Deganello

Coordinatore:
Prof. Paolo Lo Meo

Università degli Studi di Palermo

Dottorato di Ricerca in Scienze Chimiche XXIV Ciclo

Study of advanced materials for solid oxide fuel cells: influence of dopants and synthesis procedures on anode and electrolyte properties

Chiara Aliotta

Tutor:
Prof. Antonino Martorana
Co-tutor:
Dr. Francesca Deganello
Coordinatore:
Prof. Paolo Lo Meo

A Giuseppe,
mio complice in ogni avventura: sono
per te questi tre anni della mia vita.

A mia sorella che ogni giorno
mi ricorda di ricercare la bellezza.

Ai miei genitori che mi hanno
insegnato a mettere passione
in ogni cosa.

...la forma delle cose si distingue
meglio in lontananza.

I. Calvino

Contents

Abbreviations and symbols 3

Motivation 7

1) Introduction

1.1 Solid Oxide Fuel Cells 9

2) Ln-CeO$_{2-x}$: electrolytes for IT-SOFC

2.1 Pure CeO$_2$ 15

2.2 Lanthanides doped ceria, Ln-CeO$_{2-x}$ 19

2.3 Space charge model 21

3) Ce$_{0.8}$Sm$_{0.2}$O$_{2-x}$: results and discussion

3.1 Synthesis 27

3.2 Fuel-mixtures effects on structure and microstructure 30

3.3 Fuel-mixtures effects on conductivity 34

3.4 Conclusion 37

4) Ln-CeO$_{2-x}$: results and discussion

4.1 Synthesis 39

4.2 Structural characterization 40

4.3 Electrical properties 50

4.4 Conclusion 58

5) $La_{1-x}Sr_xCr_{1-y}Fe_yO_{3-\delta}$: anodes for IT-SOFC

5.1 Structure and defect chemistry of $LaCrO_3$ 59
5.2 Electrical properties 62

6) $La_{1-x}Sr_xCr_{1-y}Fe_yO_{3-\delta}$: results and discussion

6.1 Experimental 65
6.2 Evaluation of phase composition 66
6.3 Evaluation of the reduction properties 70
6.4 Evaluation of the electrical properties 75
6.5 Conclusion 78

7) Experimental methods

7.1 Solution combustion synthesis (SCS) 79
7.2 X-Ray powder Diffraction (XRD) 80
7.3 Extended X-ray Absorption Fine Structure (EXAFS) 80
7.4 Microscopy 81
7.5 Nitrogen adsorption 81
7.6 Four Point Probe - Van der Pauw method 81
7.7 Temperature Programmed Reduction (TPR) 82
7.8 Electrochemical Impedance Spectroscopy (EIS) 82

Summary 85

References 87

Acknowledgements 97

Curriculum vitae 99

Abbreviations and symbols

List of abbreviations

AC	Alternating current
BLM	Brick layer model
DC	Direct current
EIS	Electrochemical impedance spectroscopy
EXAFS	Extended X-ray absorption fine structure
FC	Fuel cell
GB	Grain boundary
GDC	Gadolinia doped ceria
HT	High temperature
IT	Intermediate temperature
MEA	Membrane electrode assemblies
PC	Proton conductor
RC	Resistance-capacitor circuit
SCL	Space charge layer
SCS	Solution combustion synthesis
SDC	Samaria doped ceria
SEM	Scanning electron microscopy
SOFC	Solid oxide fuel cell
TPB	Three phase boundary
XRD	X-ray diffraction
YSZ	Yttria stabilized zirconia

List of symbols

a	Unit cell parameter
A_s	Surface area
c	Defect concentration
C	Capacitance
C_b	Bulk capacitance
C_{gb}	Grain boundary capacitance
$d\%$	Relative density
δ	Oxygen defectivity in perovskite-type oxide
E	Activation energy
E_a	Association energy
E_m	Migration energy
e	Charge of electron
ε_0	Vacuum dielectric constant
ε_r	Specific dielectric constant
ϕ	Electrostatic potential
$\Delta\phi$	Electrostatic potential in relation to the bulk
$\Delta\phi_0$	Space charge potential
φ	Reducers-oxidizers ratio
ΔG	Free energy of Gibbs
$h^\bullet$	Electron hole
K	Constant of equilibrium
k	Boltzmann constant
Ln	Lanthanide
λ^*	Space charge layer width
$\Delta L/L_0$	Linear shrinkage
l_{XRD}	Crystal size determined by X-ray diffraction
m	Dopant concentration
Mw	Molar wheight

μ	Mobility
μ_k	Electrochemical potential
μ^0	Standard chemical potential
N	Coordination number
PO_2	Partial oxygen pressure
Q	Constant phase element
Q_{CD}	Local charge density
r	Ionic radius
r_c	Critical ionic radius
Δr	Difference between two ionic radii
R_b	Bulk resistance
R_{gb}	Grain boundary resistance
R_t	Total resistance
$R1$	First shell distance
$R2$	Second shell distance
$R(F^2)$	Residual Rietveld factor
σ	Electrical conductivity
σ_b	Bulk conductivity
σ_e	Electronic conductivity
σ_{gb}	Grain boundary conductivity
$\sigma_{GB}^{\perp}$	Grain boundary electrical conductivity along perpendicular paths
σ_i	Ionic conductivity
σ_p	Conductivity of negative carriers
σ_o	Pre-exponential factor
σ_p	Conductivity of positive carriers
σ_t	Total conductivity
σ^2	Debye-Waller factor
τ	Goldschmidt tolerance factor
τ_{b}	Bulk relaxation time constant

τ_{gb}	Grain boundary relaxation time constant
$V_O^{\bullet\bullet}$	Oxygen vacancy
wF/M	Weighted fuel-to-metal cations ratio
z	Effective charge
Δz	Difference between ionic charges
Z	Impedance
ImZ	Imaginary part of impedance
ReZ	Real part of impedance

Motivation

Today fuel cell (FC) technology is envisaged as a strategic alternative for providing clean energy through the exploitation of renewable sources; FC research is substantially funded by governments as a mean to meet the global market demand of zero environmental impact. Due to the high level of efficiency, FC devices are already able to compete with the existing power generation technologies and, in particular, solid oxide fuel cells (SOFCs) plants for stationary application constitute one the most efficient way to produce electric power and heat. Nowadays, the main challenges for SOFC research activity are: i) improving costs and durability, by reducing the operating temperature from ~1000°C (HT) to ~500-800°C (IT); and ii) using renewable fuels such as hydrogen and biofuels obtained by industrial and municipal wastes or energy crops. To achieve these purposes, it is essential to seek new materials characterized by suitable ionic conductivity for electrolytes and high electrocatalytic activity for electrodes. The electrolyte material must ensure high ionic conductivity, low electronic conductivity and very low permeability to both fuel and air in the operative temperature range. On the other hand, the anode material must be a mixed ionic-electronic conductor in the same temperature range, an efficient oxidation electrocatalyst and, finally, ensure good chemical and structural compatibility with the electrolyte.

In this light, the present study focuses on exploring electrolyte and anode materials for IT-SOFCs fuelled with H_2 and, as a reference for carbonaceous streams, with CH_4.

Electrolyte materials based on CeO_2 doped with samarium or gadolinium are the most promising ion oxide (O^{2-}) conductors in the intermediate range. The research activity concerning these compounds is mainly addressed to achieve the best performances in dependence of the doping amount and preparation routes. In this thesis the study of doped-CeO_2 has been divided in two different parts. In the former part, the influence of different preparation routes on the ionic conductivity of $Ce_{0.8}Sm_{0.2}O_{2-x}$ has been evaluated. In the latter, a detailed investigation on local structure in Er-, Yb- and Sm-doped ceria has been carried out, aiming at elucidating the role of different dopants on the mechanism of ionic conduction.

Concerning the anode materials, the issues of resistance towards poisoning originated by "dirty" fuels and compatibility with the electrolyte focused the research activity on the development of new oxide materials alternative to cermets. Among other candidates, it has been recently observed that $La_{1-x}Sr_xCr_{1-y}Fe_yO_{3-\delta}$ has suitable properties as potential anode for IT-SOFCs. In this thesis $LaCrO_3$-based anode materials have been investigated relative to the issues of optimal composition, structure, mixed ionic-electronic conductivity, catalytic activity towards fuel oxidation, also with consideration for the aspect of resistance to poisoning by carbonaceous fuel.

1. Introduction

1.1 Solid Oxide Fuel Cells

Solid Oxide Fuel Cells are electrochemical devices which are able to produce electrical energy and heat. A single SOFC is formed by three key components: a cathode, an anode and an electrolyte; like all the other kinds of fuel cells, the device takes its name from the solid oxide that constitutes the electrolyte material[1-6]. A SOFC layout is reported in Fig.1.1, where an oxide ion conductor electrolyte is interposed between the two electrodes.

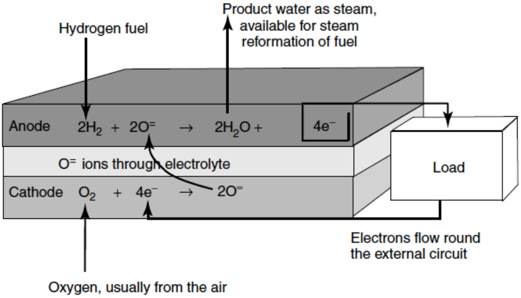
Product water as steam, available for steam reformation of fuel
Hydrogen fuel
Anode
$2H_2 + 2O^= \rightarrow 2H_2O +$
$4e^-$
$O^=$ ions through electrolyte
Cathode
$O_2 + 4e^- \rightarrow 2O^=$
Load
Electrons flow round the external circuit
Oxygen, usually from the air

Fig.1.1 Scheme of a single solid oxide fuel cell based on oxide-ion conductor as electrolyte.

In the cathode compartment oxygen, generally from air, is fed and reduced to O^{2-} ions, which migrate to the anode through the electrolyte. According to Fig.1.1, H_2 (or a different fuel) is supplied to the anode where it is oxidized providing electrons that are conveyed to the cathode through an external circuit, and producing H_2O so ensuring the accomplishment of the overall redox reaction:

$$2H_2 + O_2 = 2H_2O \qquad \text{Eq.1.1}$$

In the present work, only oxide-ion conductor electrolytes[1-10] will be treated, but it should be reminded that SOFCs with proton-conductor electrolyte (PC-SOFC) are also object of an extensive research activity[1,11,12], even if to date the development of a mature PC-SOFC technology seems not straightforward.

It is worth highlighting that the chemical nature of the electrolyte materials determines the operating temperature of fuel cells. A scheme of the main types of fuel cells is reported in Fig.1.2. Commercial SOFC devices are based on YSZ[1-3,5-10] (yttria-stabilized zirconia), fuelled with H_2 and working at ~1000°C with different configurations like the tubular design projected by the Siemens-Westinghouse or the Rolls-Royce flat-plate architecture[1-6,9,10]. High temperature SOFCs are the most efficient FC devices, with ~60-70% energy conversion efficiency of electrical power, ~20% of heat and with low emission of greenhouse gases[1-6,9-10]. For all these issues, SOFCs provide *eco*-friendly electrical current for large scale stationary distribution.

Nowadays, the research on solid oxide electrolytes is focused onto the development of materials allowing to decrease the operating temperatures from ~1000°C to an intermediate temperature[1-6,9,10] range, at about 500-800°C. Actually, the lower working temperature allows advantages in terms of overall cost, in particular due to savings in the balance-of-plant materials. Moreover, lower working temperatures enhance the device durability reducing corrosion and thermal stress. In general, both material performance and material processing should be managed to achieve satisfying IT-SOFC efficiency[9,10]. In the present work the former issue, representing a major challenge for chemistry of materials, is addressed.

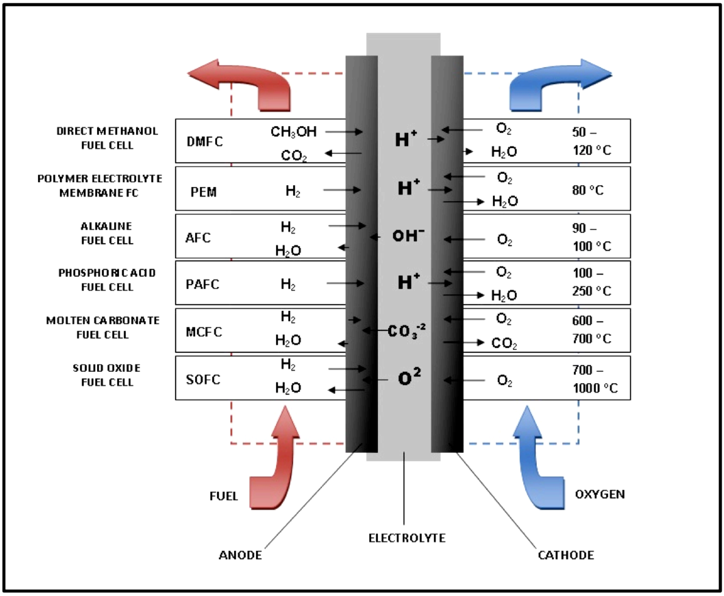
DIRECT METHANOL FUEL CELL
DMFC
CH3OH
CO2
H+
O2
H2O
50 – 120 °C
POLYMER ELECTROLYTE MEMBRANE FC
PEM
H2
H+
O2
H2O
80 °C
ALKALINE FUEL CELL
AFC
H2
H2O
OH-
O2
90 – 100 °C
PHOSPHORIC ACID FUEL CELL
PAFC
H2
H+
O2
H2O
100 – 250 °C
MOLTEN CARBONATE FUEL CELL
MCFC
H2
H2O
CO3-2
O2
CO2
600 – 700 °C
SOLID OXIDE FUEL CELL
SOFC
H2
H2O
O2
O2
700 – 1000 °C
FUEL
OXYGEN
ANODE
ELECTROLYTE
CATHODE

Fig.1.2 Summary of fuel cell types. For each FC the most used fuel and the operating temperature are reported. The chemical symbol of the electrolyte carriers is depicted associated with its own travel direction. For all FCs the oxygen is fed in the cathode compartment.

In general, the SOFC components require suitable features depending on operating temperatures, fuelling type and stack architecture. Let us consider briefly the main general issues about electrolyte and anode components.

Electrolyte. As previously mentioned, the electrolyte determines the FC operating temperature, and in the case of SOFCs must be a full density material (~90-98%) for avoiding the gases permeability. Moreover, it must exhibit essentially ionic (O^{2-}) conductivity (>0.01 Scm^{-1}) and, thus, very low or absent electronic conductivity. Besides these properties, it should have chemical stability in the working temperature range and also in the interface zones with the electrodes[1-10].

Notably, yttria-stabilized zirconia, YSZ[2,3,5,6] (Y_2O_3-ZrO_2) is employed as electrolyte of HT-SOFC, but by substituting YSZ with gadolinia-doped ceria, GDC[2,3,5,6,9-13] (Gd_2O_3-CeO_2) the working temperatures drop off in the IT-range (Fig.1.3). Nowadays, cerium oxide (CeO_2) doped with trivalent lanthanides represents the favourite candidate as electrolyte for IT-SOFCs (more details are given in chapter 2). In particular, high ionic conductivity occurs for 10-20 at.%-doping, and the most promising dopants are gadolinium and samarium[13-24]. Even though efforts have been spent to find alternative electrolyte materials, such as doped-Bi_2O_3 or doped-$LaGaO_3$, doped-CeO_2 remains the most feasible electrolyte for IT-SOFCs[3,6,9,25].

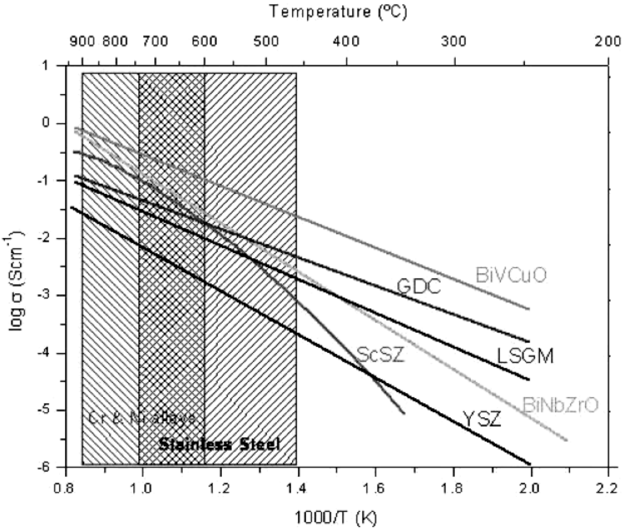

Fig.1.3 Temperature dependence of the specific conductivity for the most studied electrolyte compositions.

Anode. A good anode material should exhibit high mixed electronic-ionic conductivity, high catalytic activity for fuel oxidation, excellent chemical and thermal stability in reducing atmosphere and good compatibility with the electrolyte. Moreover, it has to be suitably porous to ensure an efficient reactants exchange and the presence of an effective three phase boundary (TPB)[2,26,27]. By considering the reaction of Eq.1.1, anodic semi-reaction involves H_2 (gas), O^{2-} and electrons which simultaneously meet in the previous mentioned TPB, which is the physical zone where the semi-reaction occurs (Fig.1.4). Thereby, TPB is the zone where gas molecules, H_2, combine with O^{2-} ions producing water and electrons.

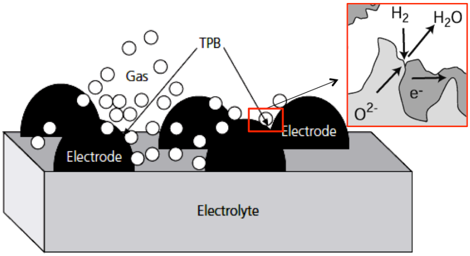

Fig.1.4 Scheme of a semi-fuel cell where TPB zones are evidenced.

The most used anode materials are constituted by a metal dispersed in a ceramic oxide, for this reason named cermets [1,2,28-30]. The oxide phase ensures the ionic transport, whereas the metal phase determines the electronic transport and electrocatalytic activity towards the fuel. The most common cermet is Ni-YSZ [3,6,31] for HT-SOFC or Ni-GDC[9,10,28,30] for IT-SOFC, that is nickel dispersed in the same material of the electrolyte. In this way, a good chemical compatibility with the electrolyte is maintained, as well as a satisfying ionic conductivity in the operating temperature range of the cell. Nevertheless, problems of homogeneity often occur. In spite Ni is a suitable electrocatalyst for hydrogen oxidation, in presence of hydrocarbons as fuels it easily undergoes coke poisoning with deleterious consequence on material durability and cell performance[9,10,28,30]. In this light, perovskite-type oxides (ABO_3), as doped-$LaMnO_3$[2-4,9,10,26,27] or doped-$SrTiO_3$[3,9], represent a valid alternative to cermets. Notably, $LaBO_3$ (B = transition metal) compounds have been widely investigated since they are characterized by high level of thermochemical stability at low PO_2 according to the sequence: $Cr > Fe > Mn > Co > Ni$ [32-34]. Hence, $LaCrO_3$ represent suitable candidates for perovskite-type oxides as potential anode materials. Actually, strontium-lanthanum chromites are intensively used as interconnector in solid fuel cell stacks thanks to their high electrical conductivity and thermal stability in both oxidant and reducing atmospheres[35-40]. Thus, by tailoring $LaCrO_3$ features with dopants, doped-lanthanum chromites could be used as anode materials for IT-SOFCs [33,34,41-57].

2. Ln-CeO_{2-x}: electrolytes for IT-SOFC

Nowadays, it is well established the paramount importance of cerium dioxide, CeO_2, in catalysis as well as in electrochemistry. In the last decades ceria has been extensively investigated for its application in catalysis, e.g. as component of three-way catalysts (TWC), which are employed for the abatement of pollutants in automotive exhaust gas[58-63]. At the same time, lanthanide doped-CeO_{2-x}[2,3,5,6-10] is widely employed in electrochemical devices as full density O^{2-} conducting electrolyte for solid oxide fuel cells working at intermediate temperature (500-800°C). In this temperature range doped-CeO_{2-x} shows a more satisfying ionic conductivity than yttria-stabilised zirconia (YSZ)[2,3,5,6], which effectively works over 900°C. In this light the aim of the present chapter consists in summarizing briefly the electrical features of this class of materials.

2.1 Pure CeO_2

CeO_2 presents a typical fluorite-like structure[64] (space group *Fm-3m*), where cerium ions (Ce^{+4}) are arranged in a cubic close-packed array, whilst oxygen ions (O^{2-}) occupy the tetrahedral interstitial holes (Fig.2.1). At room temperature its lattice parameter oscillates around the average value of 0.541(1) nm[64], but when the temperature rises the thermal expansion of the cubic cell is enhanced by the formation of Ce^{+3} ions, which have an ionic radius higher than Ce^{+4}.

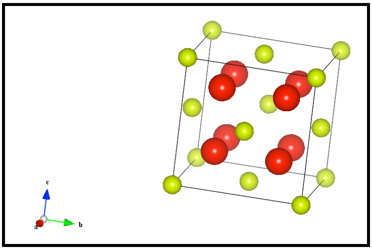

Fig.2.1 Fluorite-like structure of CeO_2. The yellow balls represent Ce^{+4}, whilst the red balls O^{2-}.

The reduction from Ce^{+4} (CeO_2) to Ce^{+3} (CeO_{2-x}) is schematized by the following equilibrium reaction, written in Kröger-Vink notation[64,65]:

$$O_O^x + 2Ce_{Ce}^x = 1/2O_2 + V_O^{\bullet\bullet} + 2Ce_{Ce}^{'} \qquad \text{Eq.2.1}$$

Ce^{+4} ions (Ce_{Ce}^x), located in their regular lattice positions, are reduced to Ce^{+3} ($Ce_{Ce}^{'}$) at the detriment of O^{2-} ions, which are released as oxygen molecules leaving oxygen vacancies ($V_O^{\bullet\bullet}$) for ensuring overall charge neutrality. Actually, the charge balance is fulfilled because two negative intrinsic defects $Ce_{Ce}^{'}$ counter balance one positive intrinsic defects $V_O^{\bullet\bullet}$, while the mass action law is ruled by the following relation[64,65]:

$$K = \left[Ce_{Ce}^{'}\right]^2 \left[V_O^{\bullet\bullet}\right] PO_2^{1/2} \qquad \text{Eq.2.2}$$

where the equilibrium constant, *K*, depends on defects concentrations and on oxygen partial pressure. By rewriting Eq.2.2 the oxygen vacancy concentration can be expressed as a -1/6 power law[64,65]:

$$\left[V_O^{\bullet\bullet}\right] = K^{'} PO_2^{-1/6} \qquad \text{Eq.2.3}$$

where K' encompasses the equilibrium constant K of Eq.2.2. Experimental determination never yields exactly the -1/6 power law, whereas this value is reasonably well approached only for high level of purity[64,66]. As the total absence of impurities is usually not attended in real systems, the exponential coefficient in Eq.2.3 differs from -1/6. This is depicted in Fig.2.2, which shows $-\Delta G(O_2)$ *vs.* $-\log(x)$, where x is the oxygen vacancy concentration.

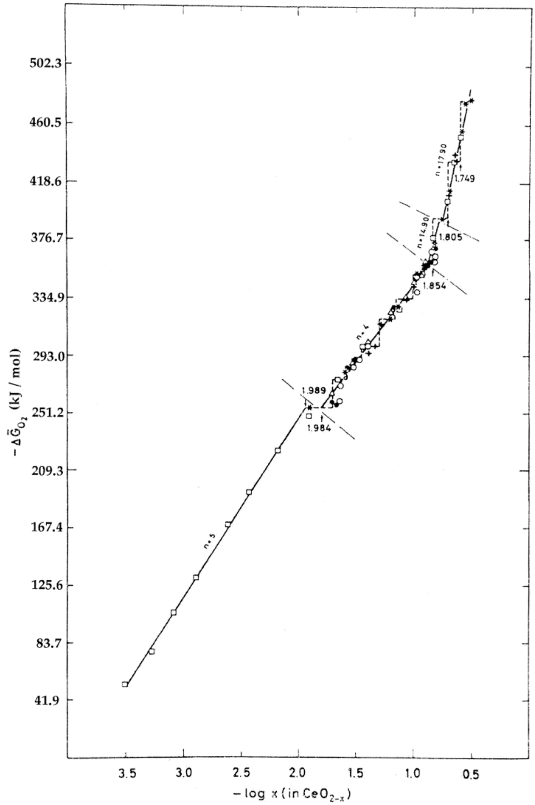

Fig.2.2 *Mogensen et al.*[64]*:* relative partial free energies ($-\Delta G(O_2)$) of CeO_{2-x} at 1100°C *vs.* composition ($\log(x)$). The parameter n is relative to the $PO_2^{-(1/n)}$ power law in Eq.2.3

In pure ceria the presence of negative $Ce_{Ce}^{'}$ defects controls the conductivity (σ) giving rise in a wide PO_2 range to *n*-type conductivity governed by the hopping of small polarons[64-66]. Actually, the ionic conductivity (σ_i) is negligible, and the conductivity is dominated by the electronic contribution σ_e:

$$\sigma_e = \left[Ce_{Ce}^{'}\right]e\mu \qquad \text{Eq. 2.4}$$

where $[Ce_{Ce}^{'}]$ and μ are respectively concentration and mobility of the negative defects Ce^{+3}, while *e* is the electron charge. It is worth noting that the hopping of the small polarons is thermally activated according to the mobility relation[64-66]:

$$\mu = (B/T)e^{-E/kT} \qquad \text{Eq. 2.5}$$

being *B* a constant and *E* the activation energy that the polarons must overcome for moving throughout the crystal.

Let us consider that $[Ce_{Ce}^{'}] = 2[V_O^{\bullet\bullet}]$, in agreement with Eq.2.1. By introducing this relation in Eq.2.4, and taking into account Eq.2.5, the dependence of σ_e on PO_2 and T is highlighted. Particularly, by rising in PO_2 the conductivity mechanism gradually changes from *n*-type to *p*-type. This is due to the following reaction:

$$V_O^{\bullet\bullet} + 1/2O_2 = O_O^X + h^{\bullet} \qquad \text{Eq.2.6}$$

where $h^{\bullet}$ are positive small polarons, also defined as positive holes[64]. As a function of oxygen partial pressure the positive polarons compete with the negative polarons, and for specific high PO_2 values they are the major carriers.

2.2 Lanthanides doped ceria, Ln-CeO$_{2-x}$

Ceria is able to host lanthanides elements (*Ln*) retaining its own fluorite structure in a relative broad concentration range[64,65,67,68]. According to Vegard's rule[69,70], a linear relationship holds between unit cell parameter and dopant concentration. Actually, the presence of lanthanides dopants can expand or contract the cell parameter, *a,* according to the empirical formula proposed by Kim[71]:

$$a = 0.5413 + \sum(0.0022\Delta r_k + 0.00015\Delta z_k)m_k \qquad \text{Eq.2.7}$$

where Δr_k is the difference of ionic radii between the *k-th* dopant and Ce^{+4}, Δz_k is the respective charge difference, m_k the molar concentration of *k-th* dopant and 0.5413 is the cell parameter of pure ceria at 25°C. Then, the stretching or the shrinkage of the cell parameter depends on the dopant ionic radius r_k, and in particular on the ratio between r_k and the critical radius, r_c, that leaves unchanged the volume of the host lattice. For a trivalent dopant of ceria, $r_c = 1.038$[71].

The *Ln*-CeO$_{2-x}$ compositions could be represented as an Ln$_2$O$_3$ oxide solubilized in pure ceria, according to the following reaction[64,65]:

$$Ln_2O_3 = 2Ln'_{Ce} + V_O^{\bullet\bullet} + 3O_O^X \qquad \text{Eq.2.8}$$

Doping with trivalent lanthanides means introducing extrinsic positive defects $V_O^{\bullet\bullet}$, which enhance the ionic conductivity of these materials. Thus, the charge transport is dominated by the drift of oxygen vacancies $V_O^{\bullet\bullet}$ through the host oxide matrix. Thereby, the conductivity of *Ln*-CeO$_{2-x}$ is mainly due to the ionic contribution, σ_i, which is PO_2 independent:

$$\sigma_i = [V_O^{\bullet\bullet}]e\mu_{V_O^{\bullet\bullet}} \qquad \text{Eq.2.9}$$

where μ is the oxygen vacancy mobility which allows for the temperature dependence of ionic conductivity:

$$\sigma_i = \frac{\sigma_0}{T} e^{-E/kT} \qquad \text{Eq.2.10}$$

In Eq.2.10 σ_o is a pre-exponential factor and E the activation energy for vacancies drift corresponding to the slope of the linear relationship between $ln(\sigma T)$ and $1/T$, as shown in Fig.2.3. The activation energy E encompasses two terms: the migration energy E_m and the association energy E_a[64,65]. The former represents the energy contribution to defects mobility, whilst the latter refers to the energy associated with the formation of complexes $[Ln_{Ce}^{'} - V_O^{\bullet\bullet}]$ which block the oxygen vacancies, so hindering the ionic conductivity. The complexes have a negative effect on conductivity, especially in cases of heavily doped ceria.

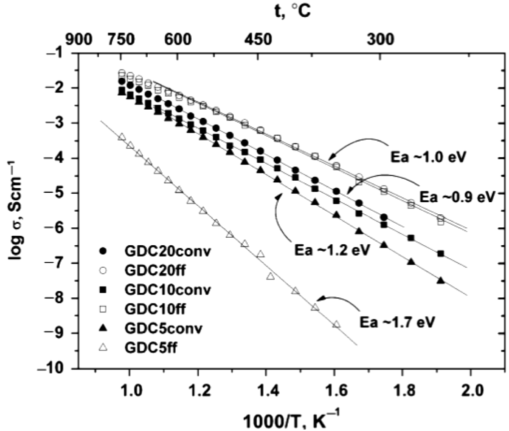

Fig.2.3 *Esposito et al.*[13]*: log (σ)-1000/T* relationships for several Gd-CeO_{2-x} compounds.

The above described analysis of conductivity in solid state Ln-CeO_{2-x} conductors is exhaustive for single crystals and for bulk materials, but does not take into account the effect of grain boundary in finely textured polycrystalline electrolytes[65-68,72-74]. In these materials the overall ionic conductivity is due to both contributions, requiring a specific treatment that is reported in the next paragraph.

2.3 Space charge model

The ionic conductivity in polycrystalline *Ln*-CeO_{2-x} electrolytes is analyzed by the space charge layer model (SCL)[75-78]. An ideal polycrystalline material can be schematized as an arrangement of evenly sized cubes representing the grains where bulk and grain boundary zones (GBs) can be recognized (Fig. 2.4)[67,79].

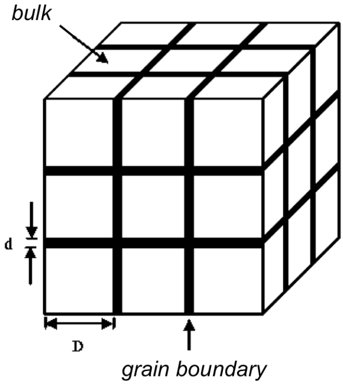

Fig.2.4 Scheme of a ideal polycrystalline material.

Grain boundaries are zones of discontinuity involving a crystallographic mismatch between adjacent, differently oriented grains, and also a different charge distribution with respect to the bulk. The GB electrostatic potential ϕ is ruled by the Poisson's equation[75,77,80]:

$$\nabla^2\phi = -\frac{Q_{CD}}{\varepsilon_0\varepsilon_r} \qquad \text{Eq.2.11}$$

where Q_{CD} is the local charge density, ε_0 the vacuum dielectric constant and ε_r the specific dielectric constant of the material. As depicted in Fig.2.5, the *"electrical"* grain boundary is formed by a core, also named interfacial core, surrounded with two adjacent space charge regions (or layers)[67,68,72,73,75-78,80,81], where the local charge density of the k-th defect is different with respect to the bulk, while the electrostatic potential bends toward the asymptotic bulk value ϕ_∞.

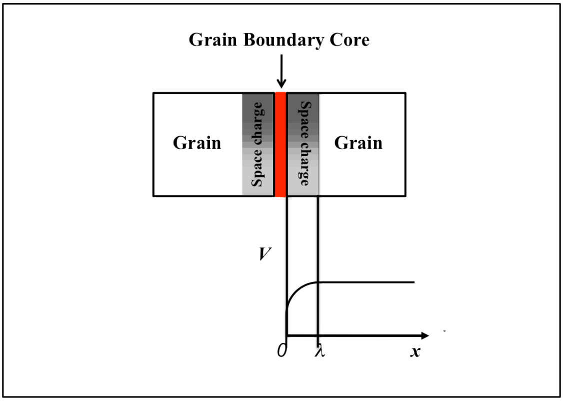

Fig. 2.5 Schematic representation of two adjacent grains. Both contribute to the mismatch zone with a space charge region, where the potential rises, and with a core, where the potential is constant.

Taking into account that in equilibrium the electrochemical potential μ_k of the defect k should be equal to the electrochemical potential of k in the bulk, $\mu_{k\infty}$, from the two equations[75-77,80]:

$$\mu_{k\infty} = \mu^o + kT\ln c_{k\infty} + z_j e\phi_\infty;$$

$$\mu_k(x) = \mu^o + kT\ln c_k(x) + z_j e\phi(x) \qquad \text{Eq.2.12}$$

by rearranging, it follows:

$$\frac{c_k(x)}{c_{k\infty}} = \exp\left(-\frac{z_k e(\phi(x)-\phi_\infty)}{kT}\right) \qquad \text{Eq.2.13}$$

where c_k and $c_{k,\infty}$ are the concentration of k in x position and in the bulk, respectively, z_k is the k-th effective charge, while $\phi(x)$ and ϕ_∞ are, respectively, the electrostatic potential in the x position and in the bulk. In Eq.2.13, ruling the concentration profile in the space charge region, $\Delta\phi(x)=\phi(x)-\phi_\infty$ is the electrostatic potential relative to the bulk. $\Delta\phi$ *at* $x=0$, $\Delta\phi_0$, is the potential of the grain boundary core with respect to the bulk, also called the space charge potential (Fig.2.5)[75-78,80]. In oxides, the GB core is a region of high $V_O^{\bullet\bullet}$ concentration, determining the formation of a positive space charge potential, $\Delta\phi_0 > 0$, that forces the depletion of the mobile oxygen vacancies in the space charge regions[67,68,72,73,75-78,80,81]. At the same time the positive potential induces an increase of the electron concentration in the SCL, with a consequent enhancement of electronic conductivity. On the contrary, in the bulk the main defects are the oxygen vacancies and the conductivity is purely ionic.

By substituting Eq.2.13 in Eq.2.11, it follows:

$$\frac{\partial^2\phi(x)}{\partial x^2} = -\frac{\sum_k z_k e c_{k\infty}}{\varepsilon_0\varepsilon_r}\exp\left(-\frac{z_k e}{kT}\Delta\phi(x)\right) \qquad \text{Eq.2.14}$$

This equation can be solved by the Guy-Chapman or the Mott-Schottky approximation[71,73]. According to the latter, the mobile defects are only oxygen vacancies and electrons, while $Ln_{Ce}^{'}$ defects are fixed. Solving Eq.2.14 in the Mott-Schottky approximation allows to determine the width of the space charge layer λ^*:

$$\lambda^* = \sqrt{\frac{2\varepsilon_0\varepsilon_r\Delta\phi_0}{z_k e c_{k\infty}}} \qquad \text{Eq.2.15}$$

which, through $\Delta\phi_0$, strongly depends on the defect structure in the space charge region.

By applying an electrical field to *Ln*-CeO_{2-x} it is possible to discriminate bulk and GBs contributions, as shown in fig. 2.6[67,73,74,77]. In general, the frequency dependence of polycrystalline materials is explained by the brick layer model (BLM)[79]. According to the model, when *Ln*-CeO_{2-x} is under an electrical field both bulk and GBs determine the overall conductivity, but, while the whole bulk is considered, perpendicular (⊥) and parallel (||) GBs are recognized (Fig.2.6). Actually, a single contribution is represented by a resistance set in series with a capacitor (*RC element*). Since the depletion in the space charge layers, the $GBs_{||}$ are negligible (Fig.2.6) compared to $GBs_{\perp}$, and the electrical behaviour of *Ln*-CeO_{2-x} can be schematized by two *RC* circuits *series* (Fig.2.6-1)[67,79,81].

The $GBs_{\perp}$ conductivity depends on the average GB thickness that λ^*, in agreement with the Mott-Schottky approximation, as follows:

$$\sigma_{GB}^{\perp} = \frac{1}{\lambda^*}\int_0^{\lambda^*} \frac{1}{\sigma_{GB}^{\perp}(x)}dx \qquad \text{Eq.2.16}$$

Generally, this perpendicular GBs contribution disappears at relative high temperature, whereas in low T range it exhibits a significant weight on the overall conductivity.

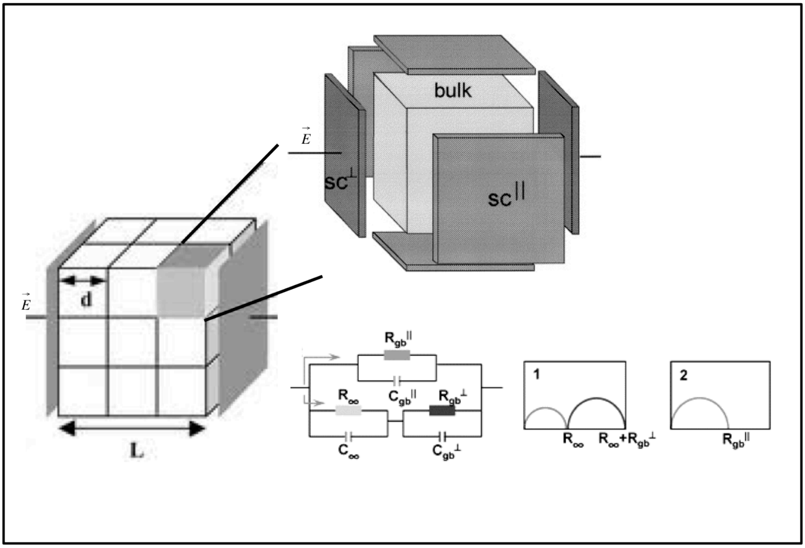
bulk
$\vec{E}$
sc⊥
sc||
$\vec{E}$
d
L
$R_{gb}^{\parallel}$
R_{∞}
$C_{gb}^{\parallel}$
$R_{gb}^{\perp}$
C_{∞}
$C_{gb}^{\perp}$
1
R_{∞}
$R_{\infty}+R_{gb}^{\perp}$
2
$R_{gb}^{\parallel}$

Fig.2.6 Schematic representation of the brick layer model for a polycrystalline *Ln*-CeO_{2-x}. A single grain is constituted by bulk and perpendicular and parallel GBs. The equivalent circuit representation of the grain is reported. The parallel GBs ($sc^{\parallel}$) are negligible, while bulk and perpendicular GBs ($sc^{\perp}$) determine the total resistance of the system ($R_{\infty}+R_{gb}^{\perp}$).

3. $Ce_{0.8}Sm_{0.2}O_{2-x}$: results and discussion

One of the main challenges for the ceria-based electrolytes is to enhance the total ionic conductivity by decreasing the resistivity of the grain boundaries at working IT-SOFC temperature. As a matter of fact, GBs affect negatively the overall ionic conductivity of doped ceria [13,67,68,74,82-85]. Owing to this, the intrinsic properties of the grain boundaries[67,68,74], as well as the sintering capacity (densification) of materials, represent key elements for improving the final electrical performance of doped-CeO_{2-x}[13,86-96]. First of all, both aspects can be controlled by an accurate choice of the dopant, and, as it is widely known, samarium is one of the most promising dopant for this class of electrolyte materials [64,65,90,97-100.] Furthermore, by shaping microstructure and morphology of the powder, it is possible to perform a material with specific electrical features[82-104]. This purpose is achieved through suitable synthesis and processing conditions, and, in this light, solution combustion synthesis (SCS) represents a flexible method to produce ultra fine powders with suitable microstructural properties[92,95,104-121]. The aim of this section is evaluating the effect of the synthesis fuels on microstructural features and, as a consequence, on ionic transport properties of $Ce_{0.8}Sm_{0.2}O_{2-x}$.

3.1 Synthesis

$Ce_{0.8}Sm_{0.2}O_{2-x}$ (SDC) was prepared by solution combustion synthesis using cerium (III) nitrate, $Ce(NO_3)_3 \cdot 6H_2O$ (99,99% Sigma-Aldrich), and samarium nitrate, $Sm(NO_3)_2 \cdot 6H_2O$ (99,99% Sigma-Aldrich), as metal precursors. 1. citric acid (99,5% Sigma-Aldrich) with ammonia, 2. cellulose (Sigma-Aldrich) with citric acid (2:1 molar ratio), 3. sucrose (ERIDANIA) and 4. sucrose with polyethylene glycol, (PEG, Mw 20000) (1:1 molar ratio), were used as combustion fuel-mixtures. Metal nitrates, fuel mixture and additive (NH_4NO_3) were dissolved in a stainless steel beaker with distilled water. The reducers-oxidizers mixture was stirred at 80°C until a gel was formed. The temperature was increased until a white dendritic powder was obtained. Temperature-time profiles were registered during the combustion process by using a K-type thermocouple. The obtained powders, called SDC1, SDC2, SDC3 and SDC4 according to the fuel mixture used for the synthesis, were then fired for 5h at 1000°C. Finally, the powders were isostatically (uniaxally) pressed and sintered in air at 1400°C for 8 hours, so obtaining pellets with a diameter of ~8 mm and a thickness of ~3 mm. Another set of pellets was obtained by sintering in H_2/Ar (4vol%) at 1400°C for 4 hours.

Four different eco-friendly combustion fuel-mixtures were chosen in this work. These fuel mixtures display different chelating ability toward the metal precursors, different microstructural templating ability and different reducing powers. Detailed information is reported in the following paragraphs.

3.1.1 Citric acid-aided SCS

The auto-combustion of citric acid in the presence of metal nitrates is largely used to prepare inorganic nanopowders because citric acid, a tri-dentate chelating agent ($pK_1 \cong 3.1$; $pK_2 \cong 4.8$; $pK_3 \cong 6.4$), is able to complex most of the metal ions by its three carboxylic functional groups [105,106,108,111,119-121]. In order to ensure the dissociation of the carboxylic groups, the pH of the solution was adjusted to ~6 with ammonia solution. During citric acid-aided SCS a white yellow gel was produced.

3.1.2 Cellulose-aided SCS

Cellulose is not a common fuel for solution combustion synthesis, probably because it is water insoluble. In the form of paper or cotton fibres activated by nitric acid it is known in literature for the production of nanopowders [122,123]. Cellulose in the presence of citric acid was recently used for preparing Sr and Fe-doped $BaCoO_3$ as IT-SOFC cathode materials[107]. It links metal ions through its hydrophobic and hydrophilic functional groups creating in water solution a network more complex than the one created by a simple complexation as in the case of citric acid. Despite of repulsion between water and hydrophobic groups metal solution remains blocked into the network favouring the gel formation. When the gel is formed, cations are distributed into the polymeric chains in the correct positions to form the oxide during the combustion process[124].

In the present work, cellulose is used in presence of citric acid as an innovative fuel to produce Sm-doped ceria. Cellulose and citric acid in 2:1 molar ratio are able to interact forming a new fuel[103]. No ammonia was added as pH regulator for the cellulose-citric acid mixture and initial pH was found to be 2.

3.1.3 Sucrose-aided SCS

Sucrose in presence of nitric acid has been already used as a fuel for combustion synthesis[125]. Sucrose is known to be oxidized to saccharic acid, that is a very good chelating agent for metal ions[126-128]. The introduction of a polymer such as PVA is often used, since it forms a polymeric resin with saccharic acid, which improves the chemical interaction with the metal cations[126]. To my knowledge, there are no literature papers reporting sucrose as template material to produce doped-ceria.

In this work, sucrose was successfully used to form Sm-doped ceria, alone and combined with polyethylene glycol (PEG). In both cases no HNO_3 or ammonia were added and the combustion proceeded at pH 5. A caramel gel was formed during both sucrose-aided SCS.

3.1.4 Calculation of ϕ and wF/M

The most important parameter connected with SCS is the ratio φ between reducers and oxidizers in the reactants mixture. According to *Jain et al.*[129] a mixture is stoichiometrically balanced when the ratio between the total valences (p, negative) of the oxidizers and the total valences (r, positive) of the fuel is unity. In the synthesis of SDC the oxidizers are the precursors $Ce(NO_3)_3$ and $Sm(NO_3)_3$, having respectively oxidizing valences of -15. According to the atomic composition of $Ce_{0.8}Sm_{0.2}O_{2-x}$:

$$p = 0.8 \cdot (-15) + 0.2 \cdot (-15) = -15 \qquad \text{Eq.3.1}$$

while r= +18, +24, +48 for citric acid, cellulose and sucrose, respectively. In order to carry out reactions under stoichiometric conditions (φ=1), ammonium nitrate, NH_4NO_3 (oxidizing valence -5) was used as a φ regulator, as reported in the following equation:

$$0.8 \cdot (-p) + 0.2 \cdot (-p) + 2 \cdot (r) + [r \text{ of auxiliary fuel}] - n5 = 0 \qquad \text{Eq.3.2}$$

n indicates the amount of NH_4NO_3 necessary to maintain the reaction balanced.

In some cases, and especially for mixed fuels, it is convenient to introduce the weighted fuel-to-metal cations ratio (*wF/M*)[107]. This parameter takes into account that in the case of fuel mixtures also auxiliary fuel contributes to the combustion process through its own specific reducing power.

3.2 Fuel-mixtures effects on structure and microstructure

The temperature-time (*T-t*) profile is a valid *in situ* characterization technique to follow the combustion process[107,130]. For all samples, except SDC4, the evolution of the combustion temperature as a function of time is reported in Fig.3.1. Inspection of *T-t* profiles shows that the temperature increases rapidly during the combustion event for all samples except for the powder prepared with citric acid (SDC1). This means that for SDC1 the combustion proceeds more slowly than for the other fuel mixtures. The combustion process of SDC4 was so fast, and the rise of temperature was so large that the detection limit (>1000°C) of the thermocouple was overcome.

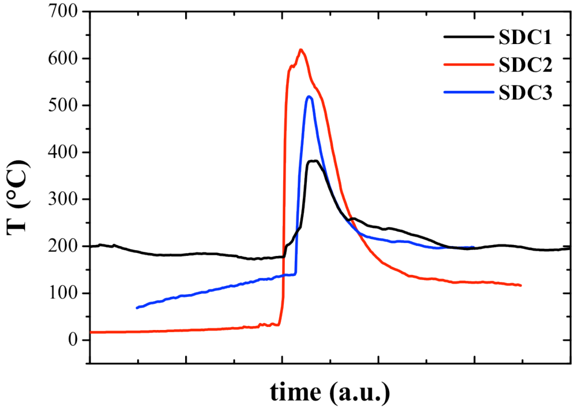

Fig.3.1 Evolution of temperature as a function of time during the combustion synthesis for SDC1 (black line) SDC2 (red line) and SDC3 (blue line).

The XRD patterns of the as prepared and calcined SDC powders show a single phase having cubic fluorite structure with cell constant, a=5.438±0.003 Å[64]. As an example, the Rietveld refined profile relative to SDC1 is reported in Fig.3.2. The absence of secondary phases suggests that the used fuel mixtures have good chelating capacity toward cerium and samarium metal cations. Since all powders exhibit quite similar (within ~10^{-3} Å) lattice constant values, it is reasonable that they have the same Sm at.% in the bulk. All specimens show slightly different crystal sizes, which could be linearly correlated with the *wF/M* ratio (Tab.3.1). The specific surface area of the sample SDC3 is definitely larger with respect to the other samples, and, to this concern, sucrose appears to be the most effective fuel. On the other hand, by inspection of Fig.3.3 and of pellet density values reported in

Tab.3.1, the sintering procedure is equally effective in reaching a high density, as evaluated with respect to the $Ce_{0.8}Sm_{0.2}O_{2-x}$ crystal density.

Tab.3.1 Weighted fuel-metals ratio (*wF/M)*, average crystallite size of calcined powders l_{XRD}, surface area (A_s), linear shrinkage ($\Delta L/L$) and relative density (*d*). Uncertainty on the last digit.

Fuel mixture	*wF/M*	*l_{XRD}, nm*	*A_S ,m^2/g*	*ΔL/L,%*	*d,%*
1-citric ac.	36	82	6.1	17.0	92
2-cellulose/citric ac.	66	92	6.0	18.5	89
3-sucrose	96	97	23.1	21.0	94
4-sucrose/PEG	116	123	1.0	19	90

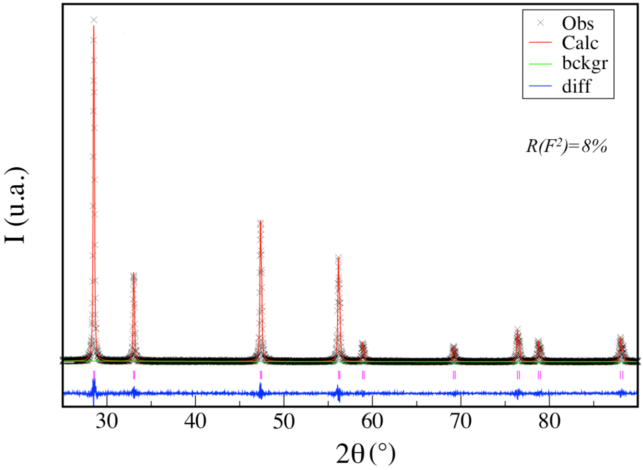

Fig.3.2 XRD data pattern and Rietveld refinement of SDC1 calcined in air at 1000°C. Black crosses: observed data; red line: calculated data; green line: background; blu line: residual. Residual Rietveld factor, R(F^2) is reported as a measure of refinement quality.

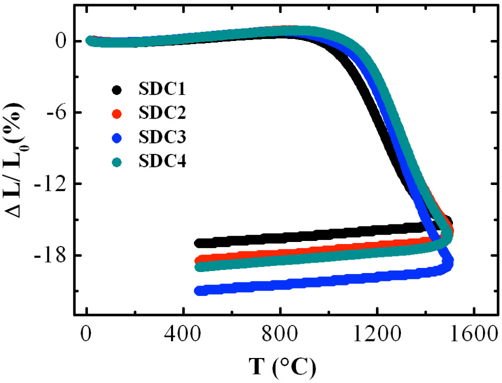

Fig.3.3 Linear shrinkage (*ΔL/L)* of $Ce_{0.8}Sm_{0.2}O_{2-x}$ cylindrical green pellets as a function of T. SDC1: black; SDC2: red; SDC3: blue and SDC4: dark cyan.

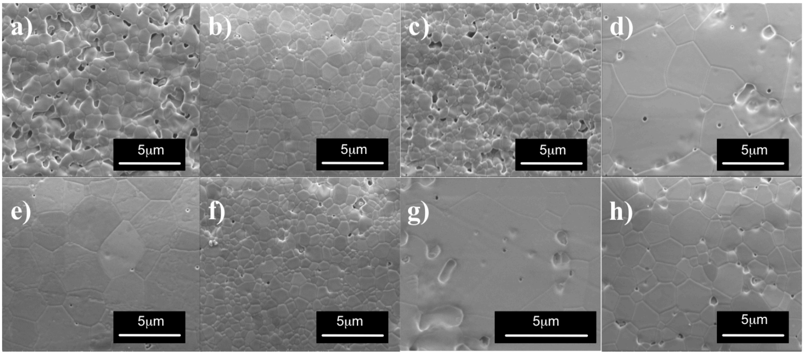

Fig.3.4 FEG-SEM micrographs of powders sinetred in air (on the top) and in H_2/Ar (4vol.%) (on the bottom). SDC1: a-e; SDC2: b-f; SDC3: c-g; and SDC4: d-h.

It is worth noting that after the different sintering treatment (air and H_2/Ar), all samples exhibit a similar cell parameter, a=5.437±0.003 Å, while the crystal sizes are encompassed between 250-310 nm. Therefore, the sintering procedure produces an about equal bulk Sm concentration and similar crystallite size in all the four investigated pellets.

The SEM images reported in Fig.3.4 elucidate the microstructural features of sintered samples in air and in H_2/Ar (4vol.%). Notably, both treatments cause the formation of open porosity, which is recognizable in all the investigated samples. After sintering in air, SDC4 shows a different morphology compared to SDC1, SDC2 and SDC3. This could be related to the low specific surface area for this sample (Tab.3.1); however, it has been reported in the literature that other features can influence the coarsening process such as dopant segregation or $V_O^{\bullet\bullet}$ mobility in the grain boundary zones[13,86]. Actually, although SDC3 shows a larger surface area with respect to SDC1 and SDC2 (Tab.3.1), the corresponding pellets are characterized by similar morphology after sintering in air (Fig.3.4). This result highlights the minor role of the powder microstructure for the densification process. Among the factors contributing to densification, it should be mentioned also the Ce^{+3}/Ce^{+4} ratio[86,88,131,132], that affects the concentration and mobility of oxygen vacancies. This parameter can be influenced by the fuel mixture, effective in stabilizing specific metal oxidation states in oxide materials for IT-SOFC[107]. Inspection of Fig.3.4 shows that sintering in reducing atmosphere produces, for sample SDC3, a striking morphology difference with respect to the sintering in air. This effect could be related to the high surface area of the SDC3 powder, corresponding to a pore structure more accessible to the reducing atmosphere. Thus, the fraction of surface Ce^{3+} and hence the increased surface oxygen vacancy concentration could enhance ionic mobility in the grain boundary region[86,88,131-132].

3.3 Fuel-mixtures effects on conductivity

The impedance spectra acquired at 260°C for all the SDC samples are reported as Nyquist plots in Fig.3.5-3.6. From high (on the left) to low (on the right) frequencies range the detected semicircles can be safely attributed to bulk, and grain boundary contributions, respectively[67,77]. In some cases the electrode response (at the utmost low frequencies) is detected. The arc intercepts with the *x*-axis permit to determine the bulk resistance (R_b), at low impedance values, and the total resistance (R_t), at high impedances range. The difference between R_t and R_b represents the grain boundary resistance (R_{gb}). The conductivity values related to each single contribution are summarized in Tab.3.2 and are determined according to Ohm's law[77].

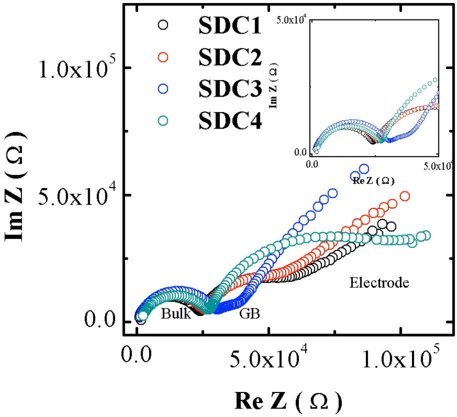

Fig.3.5 Impedance spectra acquired at 260°C relative to SDC1 (black), SDC2 (red), SDC3 (blue), SDC4 (dark cyan) sintered in air.

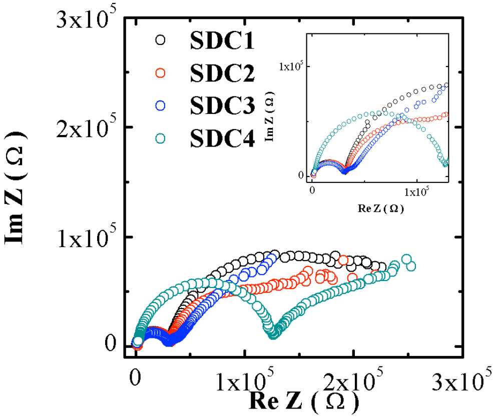

Fig.3.6 Impedance spectra acquired at 260°C relative to SDC1 (black), SDC2 (red), SDC3 (blue), SDC4 (dark cyan) sintered in H_2/Ar (4vol.%).

Tab.3.2 Total (σ_t), bulk (σ_b) and GBs (σ_{gb}) conductivity relative to the samples sintered both in air and in H_2/Ar (4vol.%). For SDC1 and SDC2 sintered in H_2/Ar only the bulk contribution is detectable. Nevertheless, it is possible to recognize qualitatively that the total and the GBs contributions are higher than the values shown by the corresponding samples sintered in air.

	σ_t, *(S/cm)*	σ_b, *(S/cm)*	σ_{gb}, *(S/cm)*
SDC1_air	$9.23\cdot10^{-6}$	$2.60\cdot10^{-5}$	$1.43\cdot10^{-5}$
SDC2_air	$8.97\cdot10^{-6}$	$2.37\cdot10^{-5}$	$1.44\cdot10^{-5}$
SDC3_air	$1.28\cdot10^{-5}$	$2.08\cdot10^{-5}$	$3.37\cdot10^{-5}$
SDC4_air	$5.41\cdot10^{-6}$	$2.24\cdot10^{-5}$	$7.14\cdot10^{-6}$
SDC1_H₂/Ar	$<9.23\cdot10^{-6}$	$1.97\cdot10^{-5}$	$<1.43\cdot10^{-5}$
SDC2_H₂/Ar	$<8.97\cdot10^{-6}$	$1.93\cdot10^{-5}$	$<1.44\cdot10^{-5}$
SDC3_H₂/Ar	$1.27\cdot10^{-5}$	$2.04\cdot10^{-5}$	$3.32\cdot10^{-5}$
SDC4_H₂/Ar	$1.79\cdot10^{-6}$	$4.91\cdot10^{-6}$	$2.83\cdot10^{-6}$

After sintering in air, the minor total resistance is relative to the sample SDC3, which is also characterized by the lowest grain boundary resistance compared to the other samples (Fig.3.5). On the contrary, SDC4 has the highest R_{gb} as well as the highest total contribution R_t (Fig.3.5). All samples have the same bulk resistivity, and thus similar bulk conductivity, in agreement with the same Sm at.% in the bulk.

Fig.3.6 shows the impedance spectra acquired after sintering in H_2/Ar (4vol.%). Again, SDC3 exhibits the lowest R_{gb}, while SDC4 the highest R_{gb}. Nevertheless, SDC4 is characterized by a notable R_b increase. It is not clear the origin of the different behaviour of this sample: some authors put forth the hypothesis that the reducing atmosphere affects the bulk distribution of the dopant and favours the formation of stable $Sm - V_O^{\bullet\bullet}$ complexes[86]. Except for SDC3, all the samples sintered in H_2/Ar (4vol.%) manifest lower total ionic conductivity compared to the corresponding samples sintered in air.

3.4 Conclusion

$Ce_{0.8}Sm_{0.2}O_{2-x}$ electrolyte prepared with different combustion fuels and sintered in air show different electrochemical properties. The material prepared with sucrose exhibits the best overall performance with a low grain boundary resistance. This points out that a careful choice of the combustion fuel is determinant for tailoring the total ionic conductivity of $Ce_{0.8}Sm_{0.2}O_{2-x}$ electrolyte. In particular, the grain boundary conductivity is considerably improved by sucrose fuel. While there is a general increase of the total resistance conductivity after H_2/Ar sintering, the experimental evidence is that the conductivity of the sample prepared with sucrose is quite unaffected by the reductive treatment. This might represent a further advantage for application as IT-SOFC electrolytes, since the electrical mismatch between anode-side and cathode-side is thus minimized.

4. *Ln*-CeO$_{2-x}$: results and discussion

As discussed in chapters 1 and 2, acceptor-doped CeO$_2$ is the best candidate as electrolyte material for IT-SOFC, and in particular Sm (III) and Gd (III) are able to enhance the ionic conductivity. Actually, several authors observed that, for lanthanide dopants, a higher ionic radius corresponds to enhanced ionic conductivity, even though this occurs until a threshold value beyond which the conductivity decreases[65,90,100]. To the best of my knowledge, there are few studies[68] regarding structural investigation about *Ln*-CeO$_{2-x}$, which focus on the correlation between structure and electrical properties although, recently, some authors reported computational approaches for studying the local structure of doped ceria[133-141]. In this context, the aim of this section consists in exploring the relations between electrical properties and local structure in (10-30 at.%) doped-ceria. For this purpose Sm (III), Er (III) and Yb (III) were selected to carry out a comparison about local structure and performances between the respective CeO$_2$-based electrolytes. All samples were prepared by SCS and sintered in air at two different temperatures (800 and 1250°C). The samples were characterized by X-ray diffraction, SEM microscopy, EXAFS and impedance spectroscopy (IS).

4.1 Synthesis

Ce$_{1-y}$*Ln*$_y$O$_{2-x}$ (*Ln*= Sm(III), Er(III); Yb(III); *y*= 0.1, 0.2, 0.3) were synthesised by solution combustion synthesis using citric acid as fuel and hydrate *Ln*(NO$_3$)$_3$ as metal precursors as reported in section 3.1 and 3.1.1. All calcined

(500°C, 5h) powders were isostatically pressed at ~200 MPa and sintered in air at 800°C for 30 minutes or at 1250°C for 10 hours with a heating rate of 5°C/min and cooling rate of 3°C/min. The final pellets sintered at 800°C had a diameter of about 6 mm and a thickness of ~1.2 mm, whereas after sintering at 1250°C pellets were characterized by a diameter of ~5 mm and a thickness of ~1 mm. $Ce_{1-y}Ln_yO_{2-x}$ compositions investigated in this work are labelled with the abbreviation *L*DC10(20;30)M(N) where *L* refers to the first letter of the dopant species Yb, Er or Sm, the number corresponds to the mole percentage of dopant concentration and the suffix M or N indicate if the compound was sintered at 1250°C or at 800°C, respectively.

4.2 Structural characterization

All $Ce_{1-y}Ln_yO_{2-x}$ specimens display the typical *Fm-3m* fluorite structure of pure ceria[64]. The Rietveld refinement was performed on green powders as well as on grinded pellets. In Fig.4.1 the XRD patterns coupled with Rietveld refinement are reported for the YDC10N specimen, selected as an example. Furthermore, the fitting parameters: lattice constant (*a*), crystal size (l_{XRD}) and R-factor ($R(F^2)$) are listed in Tab.4.1.

The insertion of trivalent lanthanide dopants into the cubic structure of ceria modifies the unit cell parameter as a function of dopant species and concentration (Fig.4.2)[65,90,100.] Samarium, which is the largest dopant with ionic radius r_{Sm}=1.079 Å[142] (8-fold coordination), expands the cubic cell, while Er (r_{Er}=1.004 Å, coord.8)[142] and Yb (r_{Yb}=0.985Å, coord.8) [142], whose ionic radii are smaller than the critical radius r_c=1.038 Å determined by Kim[71], cause the contraction.

In agreement with the Vegard's rule[69,70], for the *Sm*-CeO_{2-x}, the lattice constant rises when the Sm content increases, but it remains quite unaffected by the different sintering procedures. On the contrary, $Ce_{1-y}Er_yO_{2-x}$ and $Ce_{1-y}Yb_yO_{2-x}$

undergo unit cell contraction as a function of both dopant content and sintering temperature[90,100].

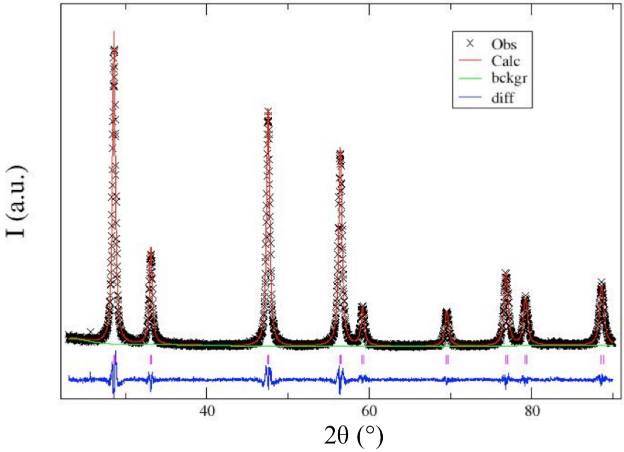

Fig.4.1 XRD pattern and Rietveld refinement of YDC10N. Black crosses: observed data; red line: calculated data; green line: background; blu line: residual.

Tab.4.1 Rietveld refinement results of the sintered specimens: unit cell constant (*a*), crystal size *l* and residual *R(F^2)*. For unit cell parameter uncertainty is referred to the last digit; for grain size is ~1%.

	a, Å	***l_{XRD}, nm***	***R(F^2)***		***a, Å***	***l_{XRD}, nm***	***R(F^2)***
SDC10M	5.4234	91	16	***SDC10N***	5.4241	23	1.9
SDC20M	5.4322	87	10	***SDC20N***	5.4334	21	2.2
SDC30M	5.4421	96	11	***SDC30N***	5.4443	22	2.7
EDC10M	5.4051	85	11	***EDC10N***	5.4085	22	2.2
EDC20M	5.3999	96	14	***EDC20N***	5.4048	21	1.9
EDC30M	5.3896	79	13	***EDC30N***	5.3992	20	2.2
YDC10M	5.3993	79	13	***YDC10N***	5.4053	21	2.5
YDC20M	5.3875	71	17	***YDC20N***	5.3966	18	1.8
YDC30M	5.3762	90	7	***YDC30N***	5.3879	17	2.4

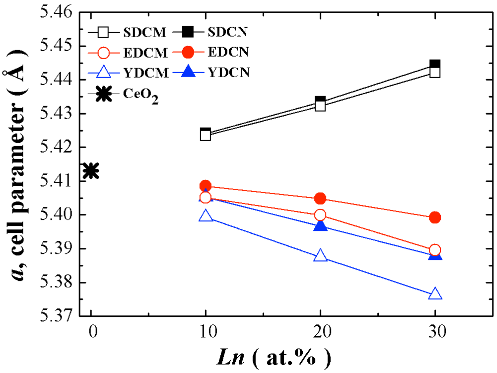

Fig.4.2 Variation of cell constant in function of dopant content compared to pure ceria lattice parameter (black star). SDCM and SDCN are represented by open and full black squares respectively. EDCM and EDCN are depicted as open and full red circles, while YDCM and YDCN are open and full blue triangles, respectively.

Fig.4.3 shows the SEM micrographs for the SDC10N and SDC10M fractured pellets. SDC10N exhibits an average grain size of ~30 nm. On the contrary, SDC10M appears dense with an average grain size ranging between about 250 nm and 1 μm.

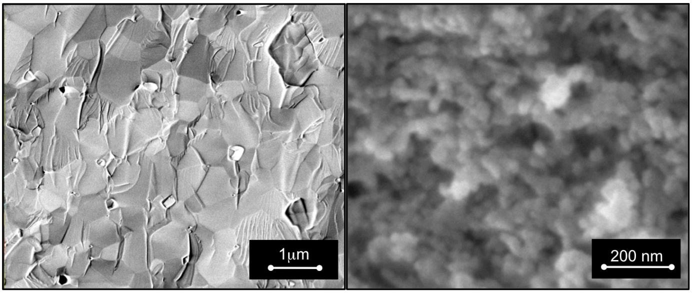

Fig.4.3 SEM micrographs of SDC10M (left) and SDC10N (right).

EXAFS spectra acquired on Ce, Yb and Er L_3 edges were suitably fitted using a structure model characterized by the *M-O* and *M-M* coordination shells of MO_2 fluorite oxide (Fig.4.4)[68,143-149]. Then, no evidence of dopant oxide segregation can be recognized. According to the fluorite-like structure, the *M* cations are surrounded by 8 oxygen atoms in the first shell (*M-O*), by 12 cations in the 2-th shell (*M-M*) and by 24 oxygen atoms in the 3-th shell (*M-O*). In order to evaluate the oxygen defectivity around the host and guest atoms, the EXAFS analyses relative to Er-CeO_{2-x} and Yb-CeO_{2-x} were carried out simultaneously on the dopant and Ce edges, with the constraint that the overall first-shell coordination numbers are equal to the oxygen stoichiometry dictated by dopant concentration[150]. For Sm-CeO_{2-x}, whose Sm edge is too short for a reliable data analysis, the first shell oxygen coordination number was allowed to vary below 8. If oxygen vacancies are randomly distributed in the anion sublattice, simple stoichiometry considerations allow to predict that this number should be 7.8 for 10at.%, 7.6 for 20at.% and 7.4 for 30at.%. The second shell *M-M* was treated taking into account average amplitudes and phases on the basis of the nominal stoichiometry and a total coordination number of 12. In any case, since the dopants are all lanthanides, the difference as scatterers between these cations and cerium is almost negligible. The third shell *M-O* coordination number was reduced in order to account for average oxygen defectivity, since local effects are reasonably unimportant at so a large distance from the absorber. As shown in Fig.4.4 for EDC, all samples were modelled considering the first three coordination shells around the absorber atom. The fitting results are summarized in Tab.4.2-4.6.

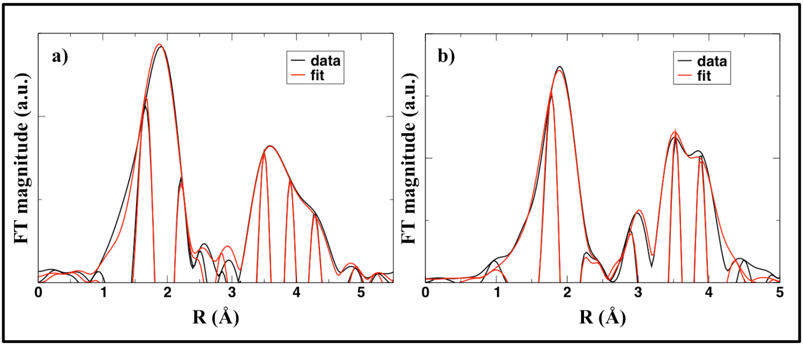

Fig.4.4 FT EXAFS data of EDC10M measured on Ce L_3-edge (a) and on Er L_3-edge (b). Black lines (moduli and imaginary parts) are the experimental data; red lines are the fitting data (moduli and imaginary parts).

Tab.4.2 Ce L_3-edge EXAFS results for EDC powders. *N:* coordination number, *R:* interatomic distance and σ^2*: Debye-Waller* disorder factor. Uncertainty on the last digit.

	Ce-O			***Ce-(Ce,M)***		
	N	***R1(Å)***	$\sigma^2(10^{-3}Å^2)$	***N***	***R2(Å)***	$\sigma^2(10^{-3}Å^2)$
CeO_2	8	2.34	5.4	12	3.81	1.6
EDC10N	7.8	2.29	5.2	12	3.83	4.8
EDC20N	7.7	2.29	9.1	12	3.81	6.5
EDC30N	7.3	2.28	8.1	12	3.79	9.1
EDC10M	7.8	2.30	6.6	12	3.81	5.0
EDC20M	7.8	2.29	8.1	12	3.80	6.6
EDC30M	7.4	2.28	9.3	12	3.79	7.9

Tab.4.3 Ce L_3-edge EXAFS results for YDC powders. *N:* coordination number, *R:* interatomic distance and σ^2*: Debye-Waller* disorder factor. Uncertainty on the last digit.

	Ce-O			***Ce-(Ce,M)***		
	N	***R1(Å)***	$\sigma^2(10^{-3}Å^2)$	***N***	***R2(Å)***	$\sigma^2(10^{-3}Å^2)$
CeO_2	8	2.34	5.4	12	3.81	1.6
YDC10N	7.8	2.30	4.1	12	3.81	3.7
YDC20N	7.6	2.29	5.6	12	3.81	5.2
YDC30N	7.5	2.27	7.2	12	3.80	7.4
YDC10M	7.8	2.30	6.4	12	3.81	4.0
YDC20M	7.6	2.28	7.4	12	3.81	5.9
YDC30M	7.6	2.28	6.6	12	3.81	8.4

Tab.4.4 Ce L_3-edge EXAFS results for SDC powders. *N:* coordination number, *R:* interatomic distance and σ^2*: Debye-Waller* disorder factor. Uncertainty on the last digit.

	Ce-O			***Ce-(Ce,M)***		
	N	***R1(Å)***	$\sigma^2(10^{-3}Å^2)$	***N***	***R2(Å)***	$\sigma^2(10^{-3}Å^2)$
CeO_2	8	2.34	5.4	12	3.81	1.6
SDC10N	7.8	2.30	5.3	12	3.81	3.7
SDC20N	7.5	2.29	6.1	12	3.81	5.2
SDC30N	7.5	2.27	7.9	12	3.80	7.4
SDC10M	7.8	2.30	6.7	12	3.81	4.0
SDC20M	7.5	2.28	6.8	12	3.81	5.9
SDC30M	7.2	2.26	8.3	12	3.81	8.4

Tab.4.5 Er L_3-edge EXAFS results for EDC powders. *N:* coordination number, *R:* interatomic distance and σ^2*: Debye-Waller* disorder factor. Uncertainty on the last digit.

	Er-O			***Er-(Ce,M)***		
	N	***R1(Å)***	$\sigma^2(10^{-3}Å^2)$	***N***	***R2(Å)***	$\sigma^2(10^{-3}Å^2)$
CeO_2	8	2.34	5.4	12	3.81	1.6
EDC10N	7.5	2.30	8.3	12	3.79	7.7
EDC20N	7.4	2.30	9.1	12	3.77	10.0
EDC30N	7.7	2.30	10.3	12	3.75	13.0
EDC10M	8.0	2.30	8.2	12	3.79	6.6
EDC20M	6.9	2.30	6.4	12	3.76	9.0
EDC30M	7.4	2.30	9.3	12	3.74	11.0

Tab.4.6 Yb L_3-edge EXAFS results for YDC powders. *N:* coordination number, *R:* interatomic distance and σ^2*: Debye-Waller* disorder factor. Uncertainty on the last digit.

	Yb-O			***Yb-(Ce,M)***		
	N	***R1(Å)***	$\sigma^2(10^{-3}Å^2)$	***N***	***R2(Å)***	$\sigma^2(10^{-3}Å^2)$
CeO₂	8	2.34	5.4	12	3.81	1.6
YDC10N	8.0	2.29	7.3	12	3.79	7.1
YDC20N	7.7	2.28	8.3	12	3.76	10.0
YDC30N	7.2	2.27	8.1	12	3.74	13.0
YDC10M	7.6	2.30	7.1	12	3.77	6.7
YDC20M	7.6	2.28	8.2	12	3.75	9.7
YDC30M	7.1	2.27	8.8	12	3.72	12.0

Coordination shell distances

Ce L_3-edge. Irrespective of dopant nature, the *Ce-O* interatomic distances are shorter compared to the values of pure ceria[68,143-145] and generally decrease by increasing the dopant concentration. As concerns the second shell, the coordination distances are much more similar to the reference CeO_2 values, but it could be for EDC, where a slight decrease with dopant content can be recognized. It is worth noticing that these EXAFS evidences are not in agreement with the XRD results (Fig.4.2), pointing to a complex long range arrangement of local structural units.

Er and Yb L_3-edges. The *M-O* and *M-(M,Ce)* interatomic distances are shorter than the corresponding 2.34 Å and 3.81Å values of pure ceria[68,143-145]. Taking into account that the ionic radii of the dopants are larger than the radius of 8-coordinated Ce^{4+}, it can be argued that the Yb and Er local arrangements are modified by oxygen vacancies and structural disorder; the latter, as results from the reported σ^2 values, is an increasing function of dopant concentration. The possibility of complex defect aggregation cannot be ruled out and could be taken into account to interpret the peculiar behaviour of Er, showing a constant first shell distance and second shell radius decreasing with dopant concentration.

First shell oxygen coordination numbers

Fig.4.5 reports a graphical overview of the first shell coordination numbers. The straight lines represent the theoretical oxygen coordination around dopant, as a function of the cerium-oxygen coordination number, under the assumption that charge balance is closely dependent on oxygen stoichiometry through the formula $Ce_{1-x}Ln_xO_{2-x/2}$. The symbols (squares and circles) are relative to the YDC and EDC samples, for which both absorption edges are available, so allowing simultaneous EXAFS analysis; the drawn error bars are probably overestimated, as they are relative to the uncertainties estimated for single-edge refinements that are strongly correlated to σ^2. For SDC, only the Ce L_3-edge is available and the corresponding coordination values are reported on the abscissas axis. It seems viable to state that, with the only exception of SDC30N, the SDC samples present a homogeneous distribution of oxygen vacancies or, even, that vacancies are preferably located in the neighbourhood of cerium. For the YDC-EDC samples, the behaviour of the “M” samples (circles) point to a tendency to homogeneous distribution or to a preferred location of vacancies near the dopant; for the “N” samples (squares), a clear trend cannot be recognized, likely due to the definitely lower sintering temperature and sintering time. The XRD results (see Fig.4.2) confirm that the “N” samples are far from an equilibrium structural arrangement.

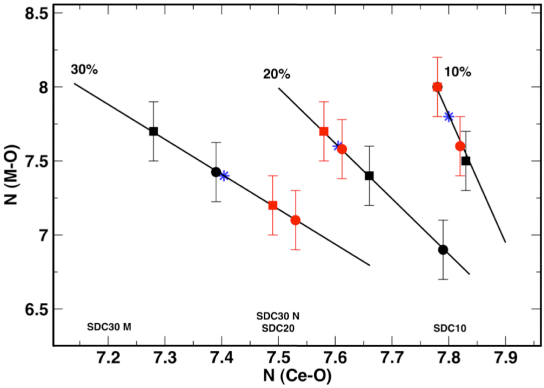

Fig.4.5 First shell coordination numbers around Ce and dopants for all samples. EDC(N-M): (black squares-black circles). YDC(N-M): (red squares-red circles). Blue asterisks represent random distribution of dopants and vacancies. For SDC(N-M) N values are reported on thex-axis.

Local environment of samarium

As above specified, the local environment of samarium could not be explored by EXAFS measurements. Nonetheless, the visible emission spectra of SDC samples provides a qualitative structural probe around Sm^{+3}, as reported in the following discussions. The Raman spectra of all samples are dominated by a sharp peak around 470 cm^{-1} (Fig.4.6), corresponding to the symmetrical stretching mode of CeO_8 unit, which is the only first-order allowed transition predicted in the whole spectrum[151-158]. The position of this peak is correlated with both the lattice and the crystal size [90,151-154]. Fig.4.6 shows the effect of the doping level on the Raman spectra of SDC and YDC prepared at 1250 °C with respect to pure CeO_2. As expected on the basis of lattice constants, the peak shifts towards lower wavenumbers for Sm^{3+} (466-468 cm^{-1}) and to higher wavenumbers for Yb^{3+} (470-473 cm^{-1}) compared to 470 cm^{-1} in pure CeO_2[90]. According to the cell parameters, the shift becomes progressively more significant with the dopant content. In the present study, the peak width increases dramatically with the dopant content rather than with crystallite size from XRD[153,154]: it can be argued that the size probed by

Raman scattering is a coherence length experimented by a phonon before being scattered by a defect, so that higher doping levels correspond to a smaller coherence length.

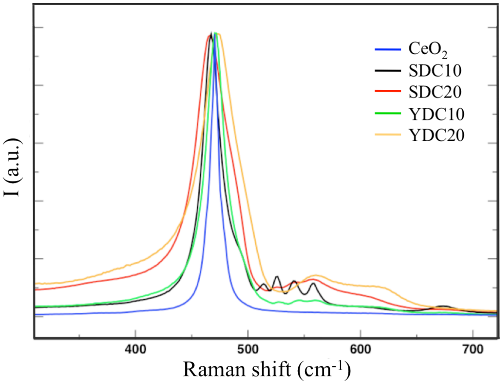

Fig.4.6 Raman spectra at 532 nm of undoped CeO$_2$ (blue), SDC10 (black), SDC20 (red), YDC10 (green) and YDC20 (orange). All samples were sintered at 1250 °C.

Two shoulders are visible around 560 and 620 cm^{-1}. Through the analysis of aliovalent-doped CeO$_2$, these features have been attributed the loosening of selection rules due to doping[90,152]. In any case, despite the large amount of trivalent dopants introduced in the fluorite lattice, a significant deviation from the average cubic symmetry is not observed. Moreover, the absence of sharp peaks around 400 cm^{-1} rules out the presence of M$_2$O$_3$ due to dopant segregation[158].

In Fig.4.7 the visible emission spectra of SDC samples are reported as structural probe around Sm^{+3}. These data are interpreted as electronic transitions of Sm^{+3} from $^4G_{5/2}$ to various ^6H states[155-157]. The peak splitting is a direct consequence of the symmetry of the crystal field, providing a qualitative structural environment around Sm^{+3}. All samples present the same features, even though the samples with lower dopant content are characterized by more resolved peaks. The SDC30N shows very broad and less defined peaks, and the bands at 560 and 575 nm disappear. The intensity ratios I($^6H_{9/2}$)/I($^6H_{5/2}$) and I($^6H_{7/2}$)/I($^6H_{5/2}$) have been previously used as a measure of the deviation from centrosymmetry in diluted

SDC[158]. In the SDC samples these ratios increase with increasing doping content and with decreasing sintering temperature, pointing out that the Sm^{+3} environment becomes increasingly asymmetric in the more concentrated samples. This is also in general agreement with the results from Raman, where lower sintering temperatures and higher doping levels increase the concentration of defects and asymmetric configurations[153,154].

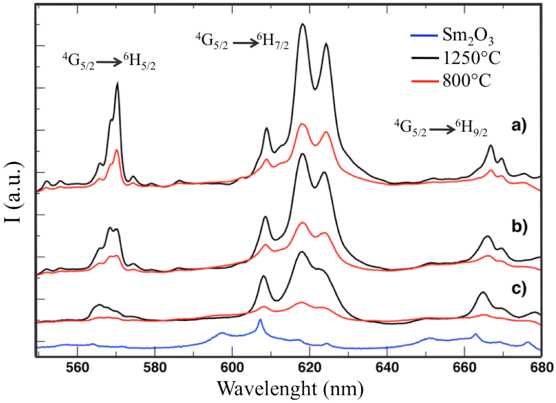

Fig.4.7 Emission spectra of SDC samples excited at laser blue 456.9 nm: a), b) and c) are 10%, 20% and 30% Sm-doped samples, respectively; black and red lines are used for samples prepared at 1250 °C and 800 °C, respectively. Sm_2O_3 is reported for comparison (blue line).

4.3 Electrical properties

The Nyquist plot of the impedance spectra collected at 400°C for $Ce_{1-y}Sm_yO_{2-x}$ and $Ce_{1-y}Er_yO_{2-x}$ (sintered at 1250°C), are shown in Fig.4.8. From these spectra three different contributions can be recognized[67,77]: (i) the high frequency intercept on the real axis corresponding to the bulk resistance, R_b (ii) the intermediate frequency arc is safely assigned to the grain boundaries, R_{gb} and (iii) the low frequency contribution corresponding to the blocking behaviour of the electrode. Note that for the 30at.% doped samples it is possible to detect an arc at high frequencies, which arises from the bulk transport. The impedance spectra were fitted with suitable equivalent circuit models consisting of one resistances

(R_b) in series with a $R_{gb}Q$ circuit, in which the equivalent phase element Q is defined as follows:

$$C = (R^{1-n}Q)^{1/n} \qquad \text{Eq.4.1}$$

where C is the capacitance and n is an additional fitting parameter weighting the capacitance contribution.

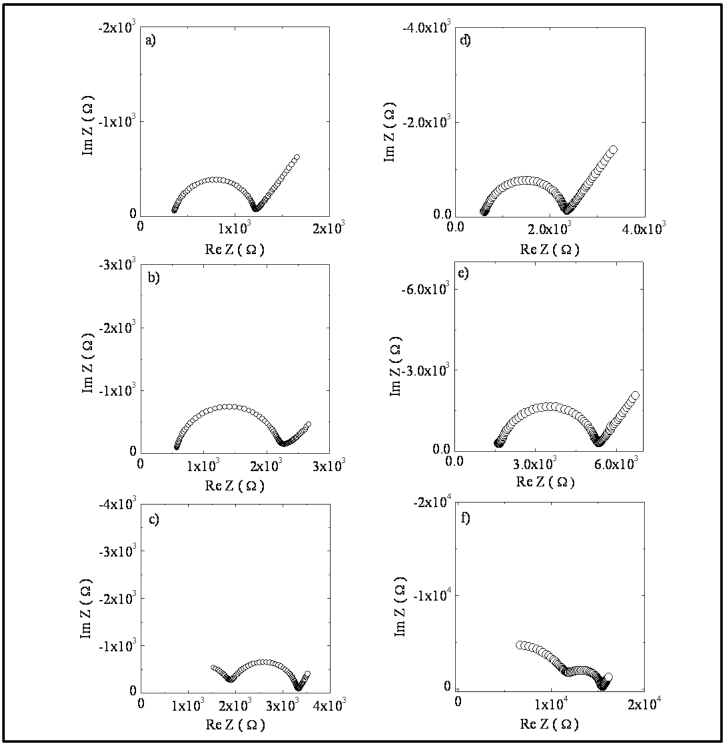

Fig.4.8 Impedance spectra collected at 400°C for SDC and EDC compositions sintered at 1250°C. On the left: a) SDC10M; b) SDC20M; c) SDC30M. On the right: d) EDC10M; e) EDC20M; f) EDC30M.

Fig.4.9 displays the impedance spectra collected at 400°C for the set of YDC and EDC compositions sintered at 800°C. For 30at.% compounds, semicircles appear depressed and convolute. This is due to similar relaxation time constants, $\tau_b = R_bC_b$ and $\tau_{gb} = R_{gb}C_{gb}$, bringing about the convolution of the respective arcs[77]. When it was possible to fit the data, one resistance R_b in series with a single $R_{gb}Q$ circuit was used as equivalent circuit model. The spectra of MDC30N could be fitted using a single RQ circuit or two RQ circuits in series[103,159]. Both models were unsatisfactory to discriminate the bulk and grain boundary contributions, and then only the total resistance was taken into account.

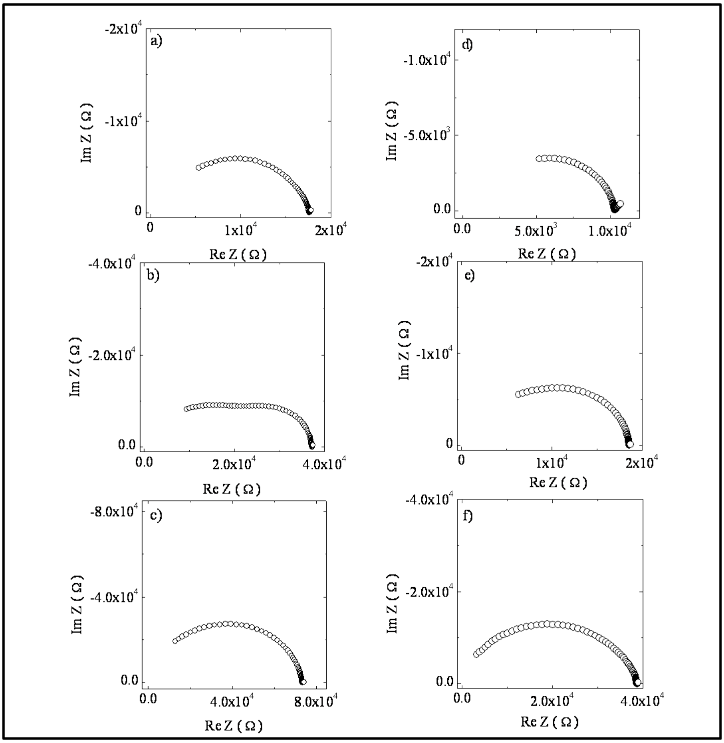

Fig.4.9 Impedance spectra collected at 300°C for YDCN and EDCN compositions. On the left: a) YDC10N; b) YDC20N; c) YDC30N. On the right: d) EDC10N; e) EDC20N; f) EDC30N.

For all samples the total (σ_t), the bulk (σ_b) and the measured grain boundary (σ_{gb}) conductivity were calculated (see Tab.4.7). Moreover, by describing the microstructure of the samples according to the brick layer model the specific grain boundary conductivity is derived from:

$$\sigma_{gb}^{\perp} = \sigma_b \frac{\tau_b}{\tau_{gb}} = \frac{\varepsilon_b \varepsilon_0}{\tau_{gb}} \qquad \text{Eq.4.2}$$

where ε_0 is the vacuum permittivity, τ_b and τ_{gb} are the relaxation times constants defined previously, and ε_b the dielectric constant. Since only in some cases it has been possible to estimate C_b, $\sigma_{gb}^{\perp}$ values have been determined by assuming the ε_b equal to 25 [67,81].

For heavily doped ceria (≥10at.%), total and bulk conductivities (Tab.4.7) depend on dopant concentration and $V_O^{\bullet\bullet}$ mobility; actually, both σ_t and σ_b drop off simultaneously as the dopant concentration increases[65,74], so that the benefits due to a higher $V_O^{\bullet\bullet}$ concentration are lost. This evidence might be attributed to limited mobility of vacancies in heavily doped ceria. For the samples containing the same dopant concentration, the differences in σ_b can be due to a different $V_O^{\bullet\bullet}$ mobility, which is affected by the dopant nature[65,], as well as by different associates, e.g. $Ln_{Ce}^{'} - V_O^{\bullet\bullet}$, which can reduce the number of mobile oxygen vacancies[72]. The different activation energies for samples with the same nominal acceptor concentration are consistent with these explanations (Tab.4.8). As expected, Sm-CeO_{2-x} compounds show higher conductivities compared to Er-CeO_{2-x} and Yb-CeO_{2-x}[65]. The different electrical performances of *Ln*-CeO_{2-x} are usually related to the ionic radii of the dopant[65,90,100] but, in the light of EXAFS results, also the local structural features affect the ionic conductivity. In this respect, the tendency of oxygen vacancies to be attracted by the dopant, particularly clear in the EDCM and YDCM samples, could be related to a strong interaction ($Ln_{Ce}^{'} - V_{O}^{\bullet\bullet}$) between positive and negative defects, and then to a reduced oxygen vacancy mobility.

Tab.4.7 Total, bulk, grain boundary and specific grain boundary conductivities acquired at 400°C.

	1250°C			
	σ_t, ***(S/cm)***	σ_b ***(S/cm)***	σ_{gb} ***(S/cm)***	$\sigma_{gb}^{\perp}$***(S/cm)***
SDC10	$3.19\cdot10^{-4}$	$1.10\cdot10^{-3}$	$4.49\cdot10^{-4}$	$1.61\cdot10^{-6}$
SDC20	$2.08\cdot10^{-4}$	$8.55\cdot10^{-4}$	$2.76\cdot10^{-4}$	$6.18\cdot10^{-7}$
SDC30	$1.01\cdot10^{-4}$	$1.77\cdot10^{-4}$	$2.37\cdot10^{-4}$	$3.68\cdot10^{-7}$
EDC10	$1.34\cdot10^{-4}$	$5.35\cdot10^{-4}$	$1.79\cdot10^{-4}$	$7.88\cdot10^{-7}$
EDC20	$7.55\cdot10^{-5}$	$2.42\cdot10^{-4}$	$1.09\cdot10^{-4}$	$2.87\cdot10^{-7}$
EDC30	$2.33\cdot10^{-5}$	$3.07\cdot10^{-5}$	$9.65\cdot10^{-5}$	$2.42\cdot10^{-7}$
YDC10	$1.45\cdot10^{-4}$	$3.70\cdot10^{-4}$	$2.38\cdot10^{-4}$	$9.35\cdot10^{-7}$
YDC20	$5.48\cdot10^{-5}$	$1.19\cdot10^{-4}$	$1.02\cdot10^{-4}$	$2.59\cdot10^{-7}$
YDC30	$2.23\cdot10^{-5}$	$2.65\cdot10^{-5}$	$1.39\cdot10^{-4}$	$2.92\cdot10^{-7}$

	800°C			
	σ_t ***(S/cm)***	σ_b ***(S/cm)***	σ_{gb} ***(S/cm)***	$\sigma_{gb}^{\perp}$***(S/cm)***
SDC10	$5.62\cdot10^{-5}$	$3.20\cdot10^{-4}$	$6.82\cdot10^{-5}$	$1.05\cdot10^{-5}$
SDC20	$6.83\cdot10^{-5}$	$2.99\cdot10^{-4}$	$8.87\cdot10^{-5}$	$1.61\cdot10^{-5}$
SDC30	$3.47\cdot10^{-5}$	-	-	-
EDC10	$3.30\cdot10^{-5}$	$2.04\cdot10^{-4}$	$3.93\cdot10^{-5}$	$1.31\cdot10^{-5}$
EDC20	$1.96\cdot10^{-5}$	$1.13\cdot10^{-4}$	$2.37\cdot10^{-5}$	$1.03\cdot10^{-5}$
EDC30	$9.25\cdot10^{-6}$	-	-	-
YDC10	$1.90\cdot10^{-5}$	$1.60\cdot10^{-4}$	$2.15\cdot10^{-5}$	$8.59\cdot10^{-6}$
YDC20	$8.86\cdot10^{-6}$	$1.57\cdot10^{-5}$	$2.04\cdot10^{-5}$	$8.73\cdot10^{-7}$
YDC30	$4.66\cdot10^{-6}$	-	-	-

Irrespective of the dopant nature, the total conductivities of MDCNs are lower than those of MDCMs, probably because the low sintering temperature favours the formation of a large volume fraction of GBs, which have a hindering effect on the ionic conductivity[67,72,74,103,159,160]. However, while σ_b are systematically lower for MDCNs with respect to MDCMs, $\sigma_{gb}^{\perp}$ of MDCNs are larger by at least one order of magnitude. This result might be due to a different spatial dopant distribution between the two series of specimens with the MDCNs having a lower bulk and a larger grain boundary acceptor concentration than the MDCMs. In general, the grain boundary blocking effect is remarkably reduced for high dopant concentration[74], that effectively limits the difference between bulk and total conductivity[65] (Tab.4.7). XRD results show that for Er and Yb the lattice parameters are lower for the “M” (sintered at 1250 °C) than for the “N” samples (sintered at 800 °C), pointing to a different defect arrangement as a function of sintering temperature and to the presence of strains that hinder oxygen mobility; this effect is present to a definitely lesser extent in Sm-CeO_{2-x}, likely due to a better fitting of the dopant in the ceria network.

The temperature dependence of conductivity, as reported in Fig.4.10 for SDC, allows the determination of the activation energies[72,80]. Total (E_t), bulk (E_b) and grain boundary (E_{gb}) activation energies computed between 300-400°C are listed in Tab.4.8.

According to literature[64], the bulk activation energies increase with the dopant content independently of the dopant nature. In agreement with the conductivity results, Sm is characterized by lower activation energy values compared to Er and Yb, as reported in Table 4.8.

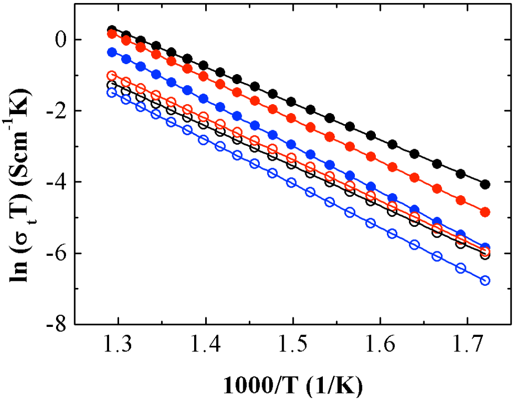

Fig.4.10 Arrhenius plots of total conductivities collected between 300-500°C for SDCM10 (full-black), SDCM20 (full-red), SDC30 (full- blue), SDC10N (open-black), SDC20N (open-red) and SDC30N (open-blue).

Tab.4.8 Activation energies determined by thermal dependence of the conductivity between 300-400°C. All values are reported in eV. Uncertainty on the last digit.

	1250°C				***800°C***			
	E_t	E_b	E_{gb}	$E_{gb,spec.}$	E_t	E_b	E_{gb}	$E_{gb,spec.}$
SDC10	0.88	0.66	0.99	0.94	0.97	0.66	1.05	0.95
SDC20	0.97	0.83	1.08	1.01	0.95	0.80	1.00	0.97
SDC30	1.11	1.10	1.15	1.16	1.07	-	-	-
EDC10	0.98	0.84	1.04	1.03	1.02	0.76	1.06	1.02
EDC20	1.09	1.05	1.18	1.11	1.08	0.95	1.10	1.05
EDC30	1.23	1.22	1.26	1.19	1.19	-	-	-
YDC10	0.97	0.81	1.07	1.02	1.04	0.91	1.05	1.09
YDC20	1.10	1.09	1.19	1.13	1.09	1.11	1.06	1.08
YDC30	1.29	1.21	1.29	0.93	1.19	-	-	-

The relation between conductivity and space charge potential (*$\Delta\phi_0$*) is ruled by:

$$\frac{\sigma_b}{\sigma_{gb}^{\perp}} = \frac{\tau_{gb}}{\tau_b} = \frac{\exp(2e\Delta\phi_0/kT)}{4e\Delta\phi_0/kT} \qquad \text{Eq.4.3}$$

The space charge potential is estimated by solving numerically Eq.4.3, and the results are listed in Tab.4.9. These values are in fair agreement with the ~0.3V established for <10at.% *Ln*-CeO_{2-x}[54,67]. It is worth noting that *$\Delta\phi_0$* for the "N" are lower than the values relative to the "M" samples [68]. This evidence is likely due to acceptor segregation in the GB core, so reducing the positive charge and then *$\Delta\phi_0$*. This result is confirmed by the bulk conductivities which are lower for MDCNs compared to MDCMs. Notably, for MDCMs increasing the dopant content the space charge potential slightly decreases according to a progressive grain boundary acceptor enrichment[161].

Tab.4.9 Space charge potential, *$\Delta\phi_0$*, dtermined at 400°C.

	1250°C	***800°C***
	$\Delta\phi_0$, V	***$\Delta\phi_0$, V***
SDC10	0.32	0.20
SDC20	0.34	0.18
SDC30	0.30	---
EDC10	0.32	0.17
EDC20	0.32	0.15
EDC30	0.25	---
YDC10	0.30	0.18
YDC20	0.30	0.19
YDC30	0.24	---

4.4 Conclusion

In this chapter the structural and electrical properties of three different ceria-based solid oxide electrolytes have been investigated. The conductivity data confirm that samaria-doped ceria is a better electrolyte material with respect to ytterbia and erbia-doped ceria. The XRD analysis demonstrate that the insertion of samarium in the network of ceria takes place more easily, while the EXAFS data point to a stronger interaction between dopant and oxygen vacancies in the case of Yb and Er doping with respect to Sm doping. All these evidences constitute a basis for a possible way to rationalize the role of different dopants in the O^{2-} conduction mechanism of solid oxide electrolytes.

5. $La_{1-x}Sr_xCr_{1-y}Fe_yO_{3-\delta}$: anodes for IT-SOFC

Since many years $LaCrO_3$-based materials are known as interconnectors for solid oxide fuel cells (SOFCs) for their high electrical conductivity and thermal stability in reducing atmospheres[35-40]. When chromium at B-site is partially substituted by a transition metal, they might show hydrogen or methane electro-oxidation activity at intermediate temperature, so that they have been recently investigated as potential anode materials IT-SOFCs[33,34,41-57,162-165].

5.1 Structure and defect chemistry of $LaCrO_3$

Perovskite-type oxides have the formula ABO_3, where the trivalent A ions are surrounded by twelve oxygen ions (AO_{12}), while the trivalent B atoms are located at the center of an octahedron (BO_6). A perovskite-type ideal structure displays a cubic unit cell (Fig.5.1-a), but on the basis of the nature of A and B atoms this structure can undergo lattice distortion leading to lower symmetry space groups. Orthorhombic and rhombohedral unit cells, relevant for $LaCrO_3$-based anode materials, are shown in (Fig.5.1-b-c)[166-169].

The structural stability of ABO_3 perovskites is ruled by the *Goldschmidt*[166] tolerance factor τ, defined as:

$$\tau = \frac{r_A + r_O}{\sqrt{2}(r_B + r_O)} \qquad \text{Eq.5.1}$$

where r_A, r_B and r_O are the ionic radii of A^{+3}, B^{+3} and O^{2-}, respectively. The range of stability of the perovskite structure is roughly $0.87<\tau<1.04$[170]. For $LaCrO_3$, $r_{La^{+3}} = 1.36$ Å[142], $r_{Cr^{+3}} = 0.615$ Å[142], $r_{O^{2-}} = 1.38$ Å[142] yield a τ value less than unity ($\tau = 0.969$) which favours the orthorhombic structure at room temperature.

It is worth noting that perovskite-type oxides can be simultaneously doped on the B-, as well as on the A- site, and this means that both r_A and r_B in Eq. 5.1 are modified. For $La_{1-x}Sr_xCrO_3$, where the A-site dopant Sr^{+2} has an ionic radius of 1.44 Å and the regular La^{+3} cation is smaller ($r_{La^{+3}} = 1.36$ Å), a fraction of the B-cations can undergo oxidation from Cr^{3+} ($r_{Cr^{+3}} = 0.615$ Å) to Cr^{4+} ($r_{Cr^{+4}} = 0.55$ Å) as a means to ensure the electroneutrality of the system. Then, as a consequence of Sr-doping, the τ value increases and the rhombohedral phase is favoured[49,166].

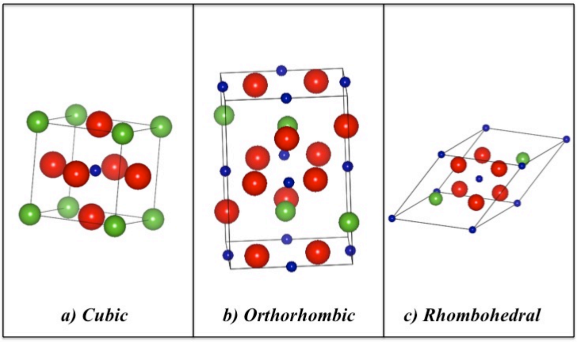

Fig.5.1 General representation of ABO_3 with a cubic (a), orthorhombic (b) and rhombohedral (c) structure. A ions are green, B blue and O red.

The presence of point defects in perovskite-type oxides is essential for tuning their electrical, magnetic, catalytic, *etc.* features. For $LaCrO_3$ the substitution of La^{3+} with Sr^{2+} ions causes the formation of oxygen vacancies, $V_O^{\bullet\bullet}$, according to the following reaction written in Kröger-Vink notation[50,51,171-173]:

$$2SrO \xrightarrow{LaCrO_3} 2Sr_{La}^{'} + 2O_O^X + V_O^{\bullet\bullet} \qquad \text{Eq.5.2}$$

where Sr^{+2} is a negative defect ($Sr_{La}^{'}$) localized in the lanthanum site, whilst the oxygen vacancy $V_O^{\bullet\bullet}$ has a twice positive charge with respect to the regular O^{2-} site occupancy. A further charge balance mechanism involved by Sr-doping entails the oxidation of a fraction of Cr^{+3} ions to Cr^{+4}:

$$2Cr_{Cr}^{X} + V_O^{\bullet\bullet} + 1/2O_2 = 2Cr_{Cr}^{\bullet} + O_O^{X} \qquad \text{Eq.5.3}$$

being Cr^{+4} a positive defect ($Cr_{Cr}^{\bullet}$) localized in the B-site. The overall charge neutrality condition is then given by:

$$\left[Sr_{La}^{'}\right] = 2\left[V_O^{\bullet\bullet}\right] + \left[Cr_{Cr}^{\bullet}\right] \qquad \text{Eq.5.4}$$

Notably, the equilibrium Eq.5.3 strongly depends on partial oxygen pressure PO_2[50,51,171,172]. Thus, taking into account the reducing atmosphere of the anode compartment (low PO_2 range) the Eq.5.3 is shifted to the left and the main source of positive defects is then accounted for by Eq.5.2. Hence, Eq.5.4 can be approximated to:

$$\left[Sr_{La}^{'}\right] \approx 2\left[V_O^{\bullet\bullet}\right] \qquad \text{Eq.5.5}$$

When also the B-site is doped with Fe^{+3}, both Fe_{Cr}^{X} and Cr_{Cr}^{X} can undergo the type of equilibrium outlined in Eq.5.3. Nevertheless, some authors[33,50], report that Cr^{+3} retains its own oxidation state, whilst Fe^{+3} is oxidized to Fe^{+4} ($Fe_{Cr}^{\bullet}$) at high PO_2 values (Eq.5.3), or reduced to Fe^{+2} ($Fe_{Cr}^{'}$) at low PO_2, according to the following reaction:

$$2Fe_{Cr}^{X} + O_O^{X} = 2Fe_{Cr}^{'} + V_O^{\bullet\bullet} + 1/2O_2 \qquad \text{Eq.5.6}$$

Therefore, by assuming that chromium remains Cr^{+3}, the condition of charge neutrality is given by the relation:

$$\left[Sr'_{La}\right]+\left[Fe'_{Fe}\right]=2\left[V_O^{\bullet\bullet}\right]+\left[Fe^{\bullet}_{Fe}\right] \qquad \text{Eq.5.7}$$

which is not exhaustive because the whole list of chemical defects includes also $Cr^{\bullet}_{Cr}$ and Cr'_{Cr}.

Since Eq.5.3. is shifted to the left at low *PO_2* range (anode regime), charge compensation involves oxygen defectivity, according to the chemical formula $La_{1-x}Sr_xCr_{1-y}Fe_yO_{3-\delta}$. The value of δ is mainly influenced by the nature of B atoms[20] whereas, for a specific composition, strongly depends on *PO_2* and T. In particular, δ values as a function of *PO_2* are depicted in Fig.5.2 for $La_{0.75}Sr_{0.25}Cr_{0.5}Fe_{0.5}O_{3-\delta}$ and $La_{0.75}Sr_{0.25}Cr_{0.5}Mn_{0.5}O_{3-\delta}$. These results obtained by Oishi *et al.*[33] show that the two compositions, which differ only for the nature of the B-site dopant, exhibit a different behaviour as concerns oxygen defectivity. Actually, doping with iron produces a quite sharp stoichiometric range, whilst for Mn-doping a larger range occurs.

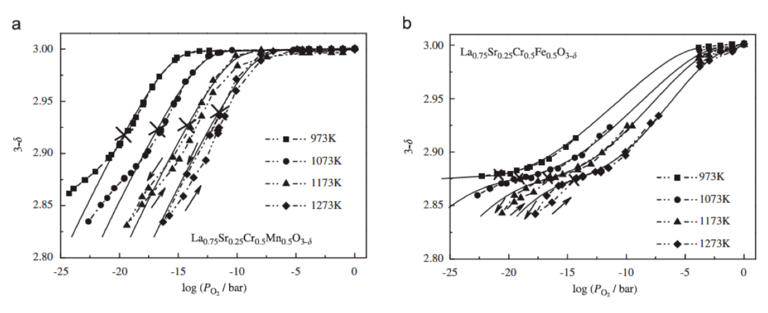

Fig.5.2 *Oishi et al.*[33]: Dependence of δ values on oxygen partial pressure for $La_{0.75}Sr_{0.25}Cr_{0.5}Mn_{0.5}O_{3-\delta}$ (a) and $La_{0.75}Sr_{0.25}Cr_{0.5}Fe_{0.5}O_{3-\delta}$ (b).

5.2 Electrical properties

As elucidated in the previous paragraph, for $La_{1-x}Sr_xCr_{1-y}Fe_yO_{3-\delta}$ the defect chemistry is ruled mainly by Eq.5.2-5.6. Actually, the electrical conductivity is strictly related to the defect equilibrium that determines the concentration of the charge carriers at specific PO_2 and T values. For the class of $LaCrO_3$-based anode materials the electrical conductivity follows a mechanism of thermally activated small polaron hopping[171,173-177]:

$$\sigma T = \sigma_0 e^{-E/kT} \qquad \text{Eq.5.8}$$

where E is the activation energy, k the Boltzmann constant and σ_o the pre-exponential factor. By plotting $log(\sigma T)$ *vs* $1/T$ (Fig.5.3), a linear trend is obtained with a slope that corresponds to the activation energy required for carriers drift throughout the matrix[171,173-177].

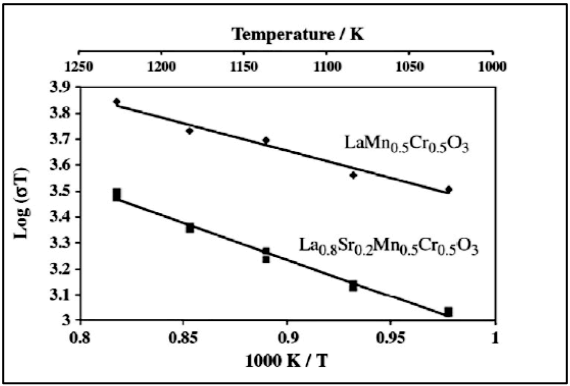

Fig.5.3 *Deleebeck[57] et al.: ln(σT)-1/T* plots for two different perovskite compounds.

Notably, an anode material exhibit a mixed ionic-electronic conductivity[54], thus *n*-type and *p*-type mechanisms are simultaneously present, and the total conductivity is:

$$\sigma_t = \sigma_n + \sigma_p \qquad \text{Eq.5.9}$$

In details, each contribution to the total conductivity can be expressed as:

$$\sigma_{n(p)} = [n(p)] e \mu_{n(p)} \qquad \text{Eq.5.10}$$

where [n(p)] are the concentration of negative or positive charge carriers and μ the corresponding charge mobility.

It is well established that in the high PO_2 range σ manifests mainly a *p*-type mechanism, since the main defects are $B_B^{\bullet}$. On the other hand, σ shifts to *n*-type for low PO_2 values, when $B_B^{'}$ are the localized carriers and the conductivity decreases with increasing in PO_2[171,173-177]. The behaviour of the electrical conductivity in a wide PO_2 range is explained by Fig.5.4, where it is clearly shown that the total conductivity is due to both σ_n and σ_p contributions. The region of the mixed conductivity is specific for each compositions and only in this light it is possible to tailor the electrical features of these compounds as anode materials.

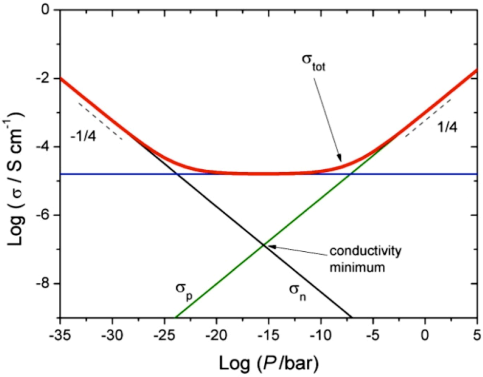

Fig.5.4 *Lupetin, P.*[80]: *Logσ-logPO$_2$* for $SrTiO_3$. Total conductivity: red line. N-type conductivity: black. P-type conductivity: green line.

6. $La_{1-x}Sr_xCr_{1-y}Fe_yO_{3-\delta}$: results and discussion

In order to extend the knowledge about the role of iron doping in $La_{1-x}Sr_xCrO_3$ compounds for their use as IT-SOFC anode materials[33,42,43,52,53], perovskite-type $La_{1-x}Sr_xCr_{1-y}Fe_yO_{3-\delta}$ ($0<x\leq0.3$; $0<y\leq0.5$) were prepared by solution combustion synthesis[53,105-107,178-182]. A careful investigation of the main properties as a function of iron doping for different Sr contents allowed us to identify a composition which represents a balanced compromise between phase purity, catalytic activity, electrical conductivity and electrochemical performance.

6.1 Experimental

6.1.1 Synthesis

$La_{1-x}Sr_xCr_{1-y}Fe_yO_{3-\delta}$ were prepared by solution combustion synthesis by using citric acid as fuel and as metal precursors $La(NO_3)_3*6H_2O$ (99,99% Sigma-Aldrich), $Sr(NO_3)_2*6H_2O$ (99,99% Sigma-Aldrich), $Cr(NO_3)_3*6H_2O$ (99,99% Sigma-Aldrich) and $Fe(NO_3)_3*6H_2O$ (99,99% Sigma-Aldrich), according to the synthesis procedure reported in the chapter 3. The reducers-oxidizers mixture was stirred at 80°C until a dark coloured gel was formed. The temperature was increased until a black fluffy powder was obtained in all doped cases, except for $LaCrO_3$ that was green. Then, the powders were fired in air for 5 hours at 1000°C or at 1100°C. Undoped lanthanum chromite, $LaCrO_3$ was named LCR, whilst the set of doped compositions $La_{1-x}Sr_xCr_{1-y}Fe_yO_{3-\delta}$ were named LCRXY, where the digits X and Y represent the corresponding dopant concentration expressed in at.%.

For the electrical measurements in d.c. the fired powders were isostatically and uniaxial pressed at 2tons/1min and then sintered at 1200°C for 1 hour. The final pellets showed a diameter of ~10 mm and a thickness of ~1.3 mm.

6.1.2 Single cell assembly

Membrane electrode assemblies (MEA) with the configuration Pt/$Ce_{0.8}Sm_{0.2}O_{2-x}$/$La_{1-x}Sr_xCr_{1-y}Fe_yO_{3-\delta}$ were assembled for carrying out electrochemical impedance spectroscopy measurements. First of all, electrolyte powders were synthesised according to the paragraphs 3.1 and 3.1.1, then dense electrolyte pellets were prepared by firing at 1400°C SDC powders isostatically pressed at 2tons/1min. A final diameter of ~19 mm and a thickness of ~1 mm were obtained. Selected $La_{1-x}Sr_xCr_{1-y}Fe_yO_{3-\delta}$ anode materials were applied on one side of SDC by slurry deposition. The slurries were prepared by mixing the powders with PEG (Mw 400) and ethanol favouring the homogenization by mixing for 1 h in ultrasonic bath. After coating one side of SDC pellet with the slurry, the assembly was pre-fired at 600°C and then sintered at 1200°C for 1 hour[105]. The other side of the assembly was coated with platinum paste and, finally, the whole MEA was pre-heated at 200°C for 30 minutes and then fired at 600°C for 1 hour.

6.2 Evaluation of phase composition

$LaCrO_3$ prepared by *SCS* and fired at 1000°C is orthorhombic (*Pbnm*)[166], and this structure is retained also after calcination at 1100°C (Fig.6.1). Doping $LaCrO_3$ with strontium brings about the formation of a multiphase compound, in agreement with the literature[166-168]. XRD measurement performed on $La_{0.9}Sr_{0.1}CrO_3$ after calcination at 1000°C show the co-existence of an orthorhombic and a rhombohedral (*R-3c*) phase with $SrCrO_4$ (*P21/c*) in traces

(Tab.6.1). The same sample calcined at 1100°C shows an increased percentage of rhombohedral phase and the disappearance of $SrCrO_4$ (Tab.6.1)[166-168]. The co-existence of both phases is maintained also in the presence of iron as clearly showed in Fig.6.2 for $La_{0.8}Sr_{0.2}Cr_{0.8}Fe_{0.2}O_3$ fired at 1100°C. In this sample it is well visible the convolution between the peaks due to orthorhombic and rhombohedral phases (inset-Fig.6.2). The Rietveld refinement permits to appreciate the small percentage of rhombohedral phase, also in those cases for which the peak convolution is not always so well resolved.

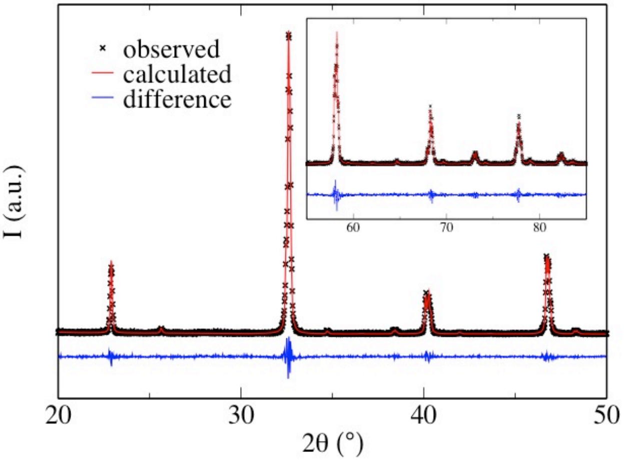

Fig.6.1 $LaCrO_3$ Rietveld refinement: observed data (black crosses), model (red line) and residual (blue line). The Rietveld residual factor, $R(F^2)$, is 13%.

Tab.6.1 Percentage phase compositions (*wt%*) with the relative volumes (*V*) for $La_{0.9}Sr_{0.1}Cr_{1-y}Fe_yO_{3-\delta}$ ($0 \leq y \leq 0.5$) sintered at 1000°C and 1100°C. $La_{0.9}Sr_{0.1}CrO_{3-\delta}$ calcined at 1000°C contains traces of $SrCrO_4$. Uncertainty is on the last digit for volume; the uncertainty for *wt%* is ≤3%.

	Orthorhombic		***Rhombohedral***	
	V (Å³)	***wt.%***	***V (Å³)***	***wt.%***
	1000°C			
$La_{0.9}Sr_{0.1}CrO_{3-\delta}$	234.04	83	350.44	16
$La_{0.9}Sr_{0.1}Cr_{0.8}Fe_{0.2}O_{3-\delta}$	235.75	76	351.13	24
$La_{0.9}Sr_{0.1}Cr_{0.7}Fe_{0.3}O_{3-\delta}$	236.30	89	353.97	11
$La_{0.9}Sr_{0.1}Cr_{0.5}Fe_{0.5}O_{3-\delta}$	237.92	100	-	-
	1100°C			
$La_{0.9}Sr_{0.1}CrO_{3-\delta}$	233.68	65	349.59	35
$La_{0.9}Sr_{0.1}Cr_{0.8}Fe_{0.2}O_{3-\delta}$	235.39	92	351.07	8
$La_{0.9}Sr_{0.1}Cr_{0.7}Fe_{0.3}O_{3-\delta}$	236.27	100	-	-
$La_{0.9}Sr_{0.1}Cr_{0.5}Fe_{0.5}O_{3-\delta}$	237.97	100	-	-

Despite the results observed for LCR2020, Fe-doping with Sr 10at.% favours the formation of orthorhombic phase as summarized in Tab.6.1; in particular, when iron amount increases the orthorhombic percentage rises as well. For these specimens, the orthorhombic and rhombohedral cell volumes linearly grow with the amount of iron due to the presence of Fe^{+3}/Fe^{+4} couple having a larger ionic radii[142] than Cr^{+3}/Cr^{+4} one. This evidence strongly suggests that iron equally enters the perovskite structure of both phases, highlighting that the chemical composition is presumably the same.

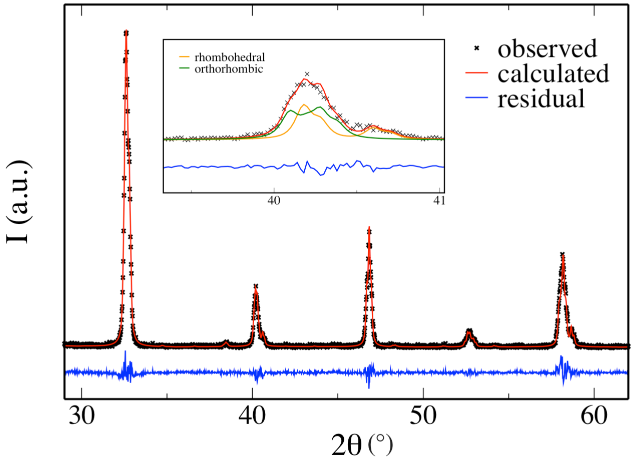

Fig.6.2 Rietveld refinement on the XRD pattern of $La_{0.8}Sr_{0.2}Cr_{0.8}Fe_{0.2}O_3$: observed data (black crosses), model (red line) and residual (blue line). In the inset: the orthorhombic (green line) and the rhombohedral (yellow line) contributions. The Rietveld residual factor, $R(F^2)$, is 15%.

By inspection of Tab.6.1 and Tab.6.2, 50at.% Fe is able to stabilize a single orthorhombic phase for Sr contents not higher than 15at.%. When the Sr concentration reaches 20at.%, the orthorhombic phase percentage drops off in favour of the rhombohedral phase with $SrCrO_4$ traces. However, beyond the 20at.% Sr doping, the orthorhombic phase is again favoured. In spite of the fact that the ionic radii of Sr(II) is 1.44 Å[142] in 12-field, and thus higher compared to 1.36 Å[142] of La(III), the cell volumes remain quite unaffected for both orthorhombic and rhombohedral phases. Probably, this is due to the fact that the introduction of a divalent ion in the A-site influences both Cr^{+3}/Cr^{+4} and Fe^{+3}/Fe^{+4} ratios, which have a direct control on the volume phase[53].

Finally, it is worth noting that the presence of $SrCrO_4$ in $La_{1-x}Sr_xCr_{0.5}Fe_{0.5}O_{3-\delta}$ $(0.2 \leq x \leq 0.3)$, is probably due to high Sr concentration which causes segregation of this Sr-rich monocline phase, when firing is carried out at temperature lower than 1100°C.

Tab.6.2 Phase and volume compositions relative to $La_{1-x}SrCr_{0.5}Fe_{0.5}O_{3-\delta}$ (0.15≤x≤0.3) sintered at 1000°C and 1100°C. Uncertainty is on the last digit for volume; the uncertainty for *wt%* is ≤3%.

	Orthorhombic		***Rhombohedral***		***$SrCrO_4$***
1000°C	***V (Å^3)***	***wt.%***	***V (Å^3)***	***wt.%***	***wt.%***
$La_{0.85}Sr_{0.15}Cr_{0.5}Fe_{0.5}O_3$	237.57	100	-	-	-
$La_{0.8}Sr_{0.2}Cr_{0.5}Fe_{0.5}O_3$	238.25	51	355.59	39	10
$La_{0.7}Sr_{0.3}Cr_{0.5}Fe_{0.5}O_3$	238.45	84	355.16	6	10
1100°C	***V (Å^3)***	***wt.%***	***V (Å^3)***	***wt.%***	
$La_{0.85}Sr_{0.15}Cr_{0.5}Fe_{0.5}O_3$	237.52	100	-	-	
$La_{0.8}Sr_{0.2}Cr_{0.5}Fe_{0.5}O_3$	238.49	82	353.69	18	
$La_{0.7}Sr_{0.3}Cr_{0.5}Fe_{0.5}O_3$	238.26	61	355.02	39	

6.3 Evaluation of the reduction properties

6.3.1 H_2-TPR

Fig. 6.3 shows the hydrogen consumption during a H_2-TPR experiment for LCR1000, LCR1030 and LCR1050. The temperature values relative to the main peak are listed in Tab.6.3 with the H_2 consumption values determined from calibrated integrated peak areas. For all samples the main peaks appear overlapped with a T_{max} at ~450°C. According to literature[183-185], it is mainly ascribable to the reduction of Cr^{+4}/Cr^{+3}, and it is firmly shaped by the presence of Sr (Fig.6.4). Since LCR (undoped) exhibits a peak with a shoulder at ~400°C, it is not possible to exclude that for the doped compositions also the reduction Cr^{+3}/Cr^{+2} occurs in this temperature range[184].

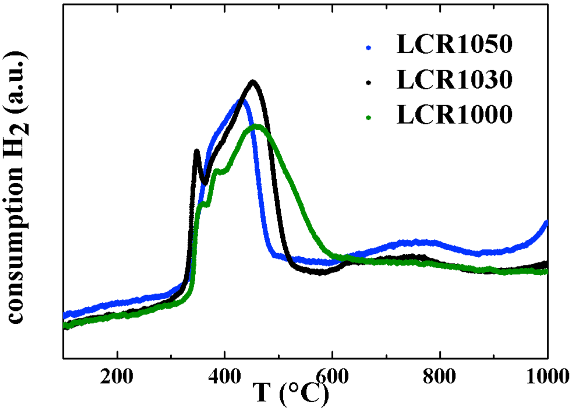

Fig.6.3 TPR profiles for LCR1050 (blue), LCR1030 (black) and LCR1000 (green).

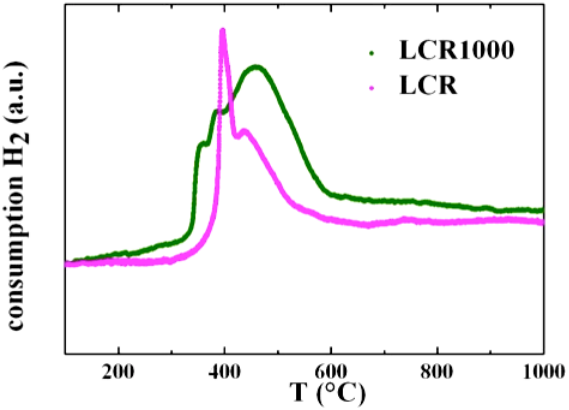

Fig.6.4 TPR profiles for LCR1000 (green) and LCR (pink).

On the other hand, the presence of iron shifts the main peak to lower temperatures (Fig.6.3) highlighting that in this temperature range, probably, both Cr and Fe are involved in the reduction processes. Effectively, *Khine et al.*[184] report for strontium doped-$LaFeO_3$ a small reduction peak at ~400°C, even though the massive Fe^{+3}/Fe^{+2} and Fe^{+2}/Fe^{0} reductions occurs at ~700°C and above 900°C, respectively. Thus, the second peak present in LCR1030 and LCR1050, as well as in LCR1550, between ~750-800°C is ascribable to $Fe(Cr)^{+3}/Fe(Cr)^{+2}$ reduction. As shown in Fig.6.5, only for LCR1550 the Fe^{+2}/Fe^{0} reduction process already begins at ~900°C, revealing a more attitude of this sample towards the H_2 oxidation.

The peak integration reveals a major H_2 consumption for LCR1000 compared to LCR1030 and LCR1050. This means that A-site doping has a major effect on reducibility, and therefore on O^{2-} availability towards the oxidation[181-183]. This is confirmed by the LCR1550 consumption compared to LCR1050; a slight variation of strontium concentration produces a notable increased reducibility of iron/chromium species. It is noteworthy that, among the investigated samples, LCR1550 exhibits the highest H_2 consumption (28.8 ml/g) between 200-1000 °C, suggesting that the highest O^{2-} availability towards oxidation process.

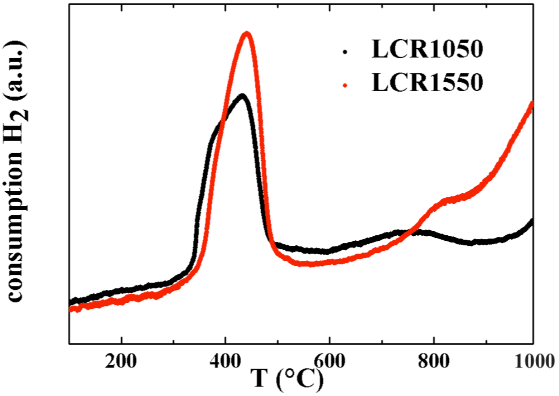

Fig.6.5 TPR profiles for LCR1050 (black) and LCR1550 (red).

Tab.6.3 List of TPR results. Temperature at maximum (T_{max}), H_2 consumption at maximum (C_{max}) and H_2 total consumption (C_t). Uncertainty for consumption is on the last digit.

	T_{max} (°C)	***C_{max} (ml/g)***	***C_t (ml/g)***
LCR	440	3.86	8.32
LCR1000	458	13.2	23.7
LCR1030	451	12.3	20.8
LCR1050	431	10.0	20.4
LCR1550	441	12.0	28.8

6.3.2 CH_4-TPR

Fig.6.6 depicts for $LaCrO_3$ and LCR1030 the consumption of CH_4 and the evolution of CO and CO_2 during a CH_4-TPR experiment. All straight lines refer to LCR1030 which is able to consume the methane through two distinct processes, occurring respectively, between 600-700°C and above 700°C, as demonstrated by the two drops off of the black straight line in Fig.6.6. The deep slope above 700°C represents the massive consumption of CH_4, through partial oxidation[42,43], according to the following reaction:

$$CH_4 + O_{ret}^{2-} = CO + 2H_2 + 2e^- \qquad \text{Eq.6.1}$$

where the oxygen ions are provided by the perovskite structure. As matter of facts, CH_4 is completely consumed only for doped-$LaCrO_3$ and full conversion is achieved within 1000°C. Moreover, in the range of temperature between 600-700°C, up to 7% of CH_4 is completely oxidized to CO_2 and water[42,43], according to the following reaction:

$$CH_4 + 4O_{ret}^{2-} = CO_2 + 2H_2O + 8e^- \qquad \text{Eq.6.2}$$

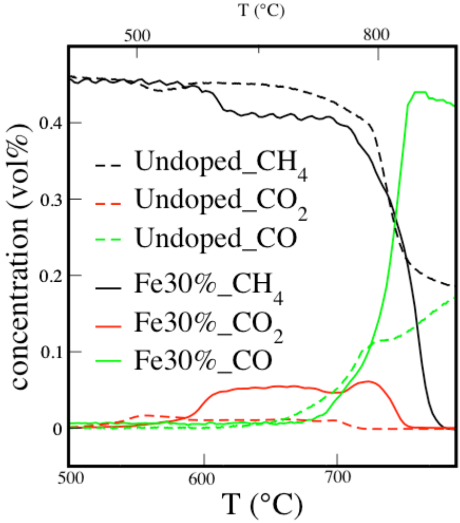

Fig.6.6 CH_4 consumption (black lines), CO_2 (red lines) and CO (green lines) evolutions during a TPR experiment between room temperature and 1000°C. LCR profiles (dashed lines) refer to the top temperature abscissas, LCR1030 profiles (straight lines) to the bottom abscissas.

This finding is common to all the doped lanthanum chromite oxides investigated in the present work and is ascribed to the presence of highly active oxygen species, likely generated by the A-site doping. Over undoped $LaCrO_3$ the CH_4 conversion starts only above 800°C with about 60% of conversion achieved at 1000°C (Fig.6.6), suggesting the poor O^{2-} availability of such sample forward methane oxidation. Furthermore, it is likely that above 850°C methane partial oxidation is associated to the side methane decomposition reaction (with coke formation and hydrogen production), in agreement with a more intense QM signal of hydrogen as compared to CO (Fig.6.7). Contrary to doped-$LaCrO_3$, the extent of total methane oxidation at around 500°C was negligible (less than 1%) (Fig.6.6).

The inspection of Fig.6.7 reveals that the partial oxidation of CH_4 is more significant for LCR1050 with respect to LCR1030, indicating a more pronounced catalytic activity forward CH_4 oxidation for the sample containing a larger iron amount[43]. It is worth underlining that different strontium concentrations do not affect the catalytic activity of doped lanthanum chromites.

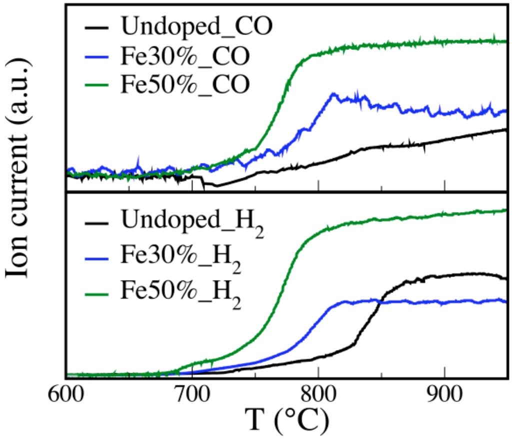

Fig.6.7 Mass quadrupole (QM) signals of H_2 (bottom) and CO (top) acquired during a TPR experiment between room temperature and 1000°C for LCR (black), LCR1030 (blue) and LCR1050 (green).

6.4 Evaluation of the electrical properties

The total conductivity of LCR1030, LCR1050 and LCR1550 is thermally activated as demonstrated by the Arrhenius plots in Fig.6.8[43]. The conductivity of LCR1550 is lower compared to LCR1030 and LCR1050, but by slightly reducing the Sr at.% a notable improvement in conductivity occurs. A similar behaviour highlights that Sr-doping influences the electronic conductivity through a direct control on the electronic bands. It is worth noting that when Sr(II) substitutes La(III) a part of the trivalent ions in B-site are forced to modify the oxidation state from +3 to +4. As a consequence the electronic bands rearrange themselves affecting the electrical conductivity[53,174-177].

On the other hand, a further gain is obtained by reducing the Fe at.%, but, despite the reduction of 20at.%, the enhancement is definitely limited[53]. It is likely that the ability of iron to improve the conductivity is reduced, probably because the band structure is not effectively modified. However LCR1030 exhibits the most satisfying electronic performance in reducing environments, probably because it represents the optimal balance between Sr- and Fe- doping.

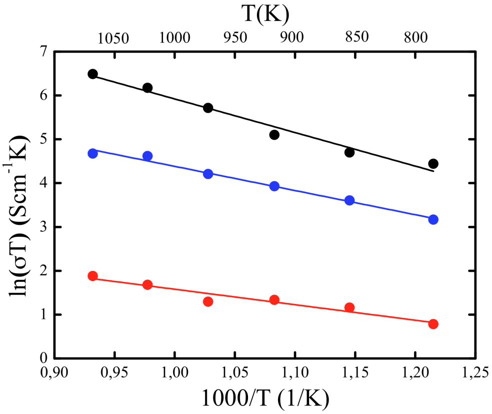

Fig.6.8 Arrhenius plots of electrical conductivity for LCR1030 (black), LCR1050 (blue) and LCR1550 (red).

Fig.6.9 shows the impedance spectra acquired at several temperatures for LCR1030[42,43,50,53] as a representative example. All spectra are characterized by a well distinguishable arc and by a piece of arc at high *Z'* values (low frequencies) that is ascribed to the Pt paste contribution. Normally, the intercept of the arc with the *x*-axis at low frequency values represents the total resistance of the cell without the contribution of the metallic electrode, whilst the intercept at high frequencies is assigned to the ohmic resistance, often named internal resistance (R_i) of the cell[43,50]. The polarization resistance R_p, resulting from the difference between the total and the internal resistances, is determined by the charge transfer process and by the gasses diffusion inside the electrode. Notably, the latter process is positively influenced by increasing temperature, as shown in Fig.6.10 for LCR1030 and LCR1550; for LCR1050 it has been possible to estimate only the R_i. Effectively, the R_p values decrease with the temperature, revealing a thermal activation for the charge and mass transfer processes, which involve the electrode materials.

The ohmic responses (R_i) are shown in Fig.6.11, and again LCR1030 exhibits definitely lower internal resistance compared to LCR1550 and LCR1050. Nevertheless, in this case the activation energies are rather similar.

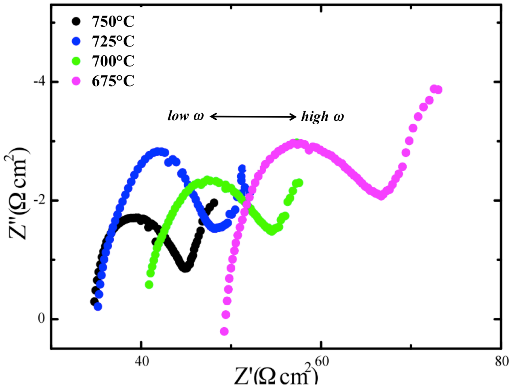

Fig.6.9 Impedance spectra acquired at several temperatures for a MEA containing LCR1030.

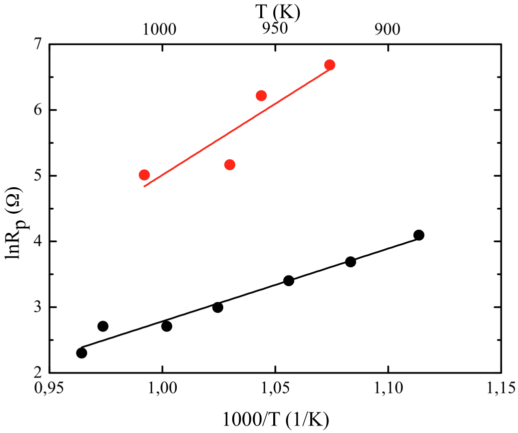

Fig.6.10 Logarithmic dependence of R_p as a function of 1/T for LCR1030 (black) and LCR1550 (red).

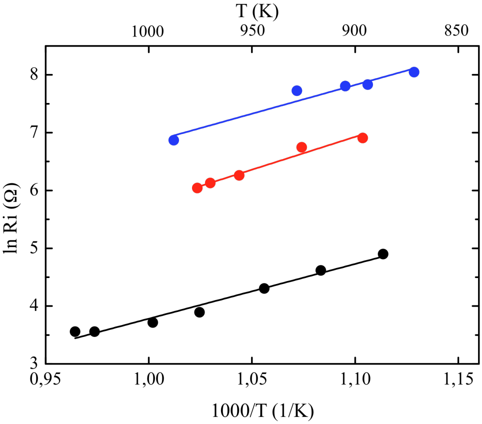

Fig.6.11 Logarithmic dependence of R_i as a function of 1/T for LCR1030 (black), LCR1550 (red) and LCR1050 (blue).

6.5 Conclusion

The perovskite oxides $La_{1-x}Sr_xCr_{1-y}Fe_yO_{3-\delta}$ ($0<x\leq 0.3$; $0<y\leq 0.5$) have been explored as potential anode for IT-SOFCs. A careful investigation of the phase purity, as a function of both Sr and Fe concentration, allowed to identify only three compositions giving pure orthorhombic phase without traces of secondary crystalline phases: specifically, $La_{0.9}Sr_{0.1}Cr_{0.5}Fe_{0.5}O_{3-\delta}$, $La_{0.85}Sr_{0.15}Cr_{0.5}Fe_{0.5}O_{3-\delta}$ and $La_{0.9}Sr_{0.1}Cr_{0.7}Fe_{0.3}O_{3-\delta}$. These materials meet the main requirements for anode materials, since they show good catalytic activity towards H_2 and CH_4 oxidation and satisfactory electrical conductivity in reducing environment. Notably, in the explored doping range, Fe doping strongly improves the catalytic activity, as well as the electrical conductivity and the phase purity. On the contrary, Sr doping ensures suitable electrical conductivity, even though it does not remarkably influence the catalytic activity. On the basis of these preliminary considerations, $La_{0.9}Sr_{0.1}Cr_{0.7}Fe_{0.3}O_{3-\delta}$ is the most promising anode material among the explored compositions because it represents the optimal compromise between phase purity, catalytic activity and electrochemical performance.

7. Experimental methods

7.1 Solution Combustion Synthesis (SCS)

Solution combustion-based methods have been successfully used in the literature for obtaining inorganic materials[53,92,95,104-121,178-182,186]. In many cases, it is simply used as an easy and fast preparation route able to compete with the classical solid-state method. Recently, several authors have explored its potentialities for obtaining materials characterized by suitable features[105-107]. The SCS is based on the propellant chemistry theory, as well as on sol-gel concepts [61,63129,186,187]. Similarly to *Pechini* method[188,189], the metal precursors react in a poor oxygen environment in presence of "fuel", a specific organic molecule such as the citric acid. The fuel has the triple role of reducer, chelating-gelling agent and microstructural template. It has been demonstrated that the fuel is able to influence phase composition, structure and microstructure of powders, but also their mechanical, electrical, catalytic, *etc*. properties[105-107].

According to the propellant chemistry principles[129], every fuel-oxidizers mixture is characterized by an intrinsic reducing power, which directly influences the combustion process. This intrinsic reducing power represent the algebraic sum of the valence of the elements constituting the organic molecules. Thus, the valences for H, C, O are +1, +4 and -2, respectively, while N carries no contribution. On this basis for example citric acid ($C_6H_8O_7$) has a reducing power of +18. In order to improve the properties of multi-component mixed oxide materials, fuel mixtures are used as well[107,120]. More detailed information are reported in chapter 3.

7.2 X-Ray powder Diffraction (XRD)

XRD measurements on the powders were carried out using a Siemens D5000 X-ray powder diffractometer, equipped with a curved graphite monochromator for the selection of the Cu Kα radiation (40kV/30mA). The step size was 0.03° 2θ for powders calcined at 500°C, while 0.02° 2θ for the specimens calcined at higher temperatures. The integration time was 3 s *per* step, and the scan range was 20-90° 2θ.

All specimens relative to chapter 6 also were analyzed using a Xpert, Philips, 3710 HTK diffractometer with a Ni-filtered Cu Kα according to the previously mentioned experimental conditions.

Rietveld refinements were performed on the diffraction patterns by using the GSAS package[190]. The peak profiles were fitted using a modified pseudo-Voigt function (CW function #3), while the background was simulated with Chebyschev polynomials (type 1). Instrumental broadening and peak asymmetry were fixed during the refinements, while lattice constants, full width at half maximum (FWHM), Debye-Waller factors and microstrain were considered as variable parameters[190-193].

7.3 Extended X-ray Absorption Fine Structure (EXAFS)

X-ray absorption measurements were carried out on Ce, Yb and Er L_3-edges at the XAFS beamline of Elettra (Trieste, Italy). The powder samples were sieved, mixed with polyvinylpyrrolidone, and pressed to form self-standing pellets. The spectra were acquired at 80K in transmission mode with a liquid nitrogen cryostat. Viper[194] and Feff9[195] were used in the EXAFS data analysis.

7.4 Microscopy

$Ce_{0.8}Sm_{0.2}O_{2-x}$. Field Emission Guns Scanning Electron Microscope (FEI Inspect F50) was employed to explore the microstructure of the sintered polished surfaces of the pellets. Polishing was sequentially made with silicon carbide powders and 15, 6, 3 and 1 μm diamond pastes. Then the pellets were cleaned with an ultrasonic bath in isopropanol. The polished specimens were thermally etched at 1300 °C for 20 min to reveal the surface grain boundaries. The experiments were performed in collaboration with Dr. R. Muccillo of the University of S. Paulo (Brazil).

Ln-CeO_2. Field Emission Scanning Electron Microscope (FE-SEM) was used to investigate the microstructure of the sintered samples. All the specimens were broken, and then they are analyzed on the fractured surface. The experiments were performed at the department of Professor J. Maier under supervision of Dr. G. Gregori of the Max Planck Institute for Solid State Research of Stuttgart (Germany).

7.5 Nitrogen adsorption

Nitrogen adsorption experiments at 77K were carried out using a Quantachrome Nova 1200 equipment. All powders were pre-treated under vacuum at 250°C for 2h. Specific surface areas were estimated with the BET method[196].

7.6 Four Point Probe - Van der Pauw method

The electrical conductivity in d.c. were performed by using the Van der Pauw method, also defined four point probes method[197]. The sample resistivity was determined by employing a potentiostat galvanostat (PAR 273 A) which supplied electrical current through two probes, and by a digital multimeter (Hewlett Packard 3457A) which measured the voltage across the other two probes with a sensibility of 1 μV. Measurements were carried out between 500-800°C in H_2(3vol.%)/Ar on pellets sintered in air for 1 hour at 1200°C. The experiments were performed in collaboration with Dr. F. Padella, Dr. C. Paoletti and Dr. E. Simonetti of the ENEA-CASACCIA of Rome (Italy).

7.7 Temperature Programmed Reduction (TPR)

Reduction properties of the perovskite oxides were studied by temperature programmed reduction (TPR) measurements between room temperature and ~1050°C (10°C/min) in H_2(vol.%)/Ar(30ml/min) and CH_4(0.45 vol.%)/He(50ml/min), respectively. Experiments were carried out with a Micromeretics Autochem 2950 instrument.

During H_2-TPR measurements, a QMS and a thermal conductivity detector (TCD) were employed for the evaluation of consumption of H_2. All powders (~0.1 g) were pre-treated before in O_2/He at 700°C and then in He for removing all absorbed species.

For CH_4-TPR experiments the inlet and outlet gas composition was analyzed by a mass quadrupole spectrometer (QMS Thermostar™, Balzers), in order to follow the evolution of all the species: CH_4, CO, CO_2, H_2, H_2O. The concentration (vol.%) of CH_4, CO and CO_2 species was measured by on line IR analyser (ABB Uras 14). The experiments were performed in collaboration with Dr. L. Liotta of the ISMN-CNR of Palermo.

7.8 Electrochemical Impedance Spectroscopy (EIS)

$Ce_{0.8}Sm_{0.2}O_{2-x}$. The impedance spectroscopy analyses were performed with a Hewlett-Packard 4192A LF Impedance Analyzer and with a series 900 HP controller in the $5\text{-}1.3\cdot10^7$ Hz frequency range. Symmetrical cells with silver electrodes were employed. Impedance spectra were acquired in air between 190-320°C and analyzed by using the Zview2 software (Scribner Associates, Inc.). The experiments were performed in collaboration with Dr. R. Muccillo of the University of S. Paulo (Brazil).

Ln-CeO*$_2$*. The electrical conductivity was measured by impedance spectroscopy (IS) using an Alpha-A high resolution dielectric analyzer (Novocontrol GmbH, Germany) in the 0.1-$1\cdot10^7$ Hz frequency range with a 0.3 V a.c. voltage. Measurements were performed in a symmetrical cell with platinum electrodes sputtered onto the surfaces of the pellets (~400 nm thickness, Edwards Auto 306 sputtering system). Impedance spectra were collected in dry pure O_2 between 300-500°C (10°C/min step-dwelling 1h), after 15 hours of equilibration, and analyzed by using the ZView2 software (Scribner Associates, Inc.). The experiments were performed at the department of Professor J. Maier under supervision of Dr. G. Gregori of the Max Planck Institute for Solid State Research of Stuttgart (Germany).

$La_{1-x}Sr_xCr_{1-y}Fe_yO_{3-\delta}$. The electrochemical impedance spectroscopy measurements were performed with SI 1260 Impedance Analyzer equipped with SI 1287 Solartron electrochemical interface in the 0.01Hz-0.1MHz frequency range. Membrane electrode assemblies (MEA) with a Pt cathode were tested at open circuit voltage between 500-750°C (5°C/min and 1-24h dwelling) with H_2 and O_2 in the anode and cathode chamber, respectively. The impedance spectra were analyzed by using the ZView2 software (Scribner Associates, Inc.) and the ZSimpWin 3.10 software. The experiments were performed in collaboration with Dr. F. Padella, Dr. C. Paoletti and Dr E.Simonetti of the ENEA-CASACCIA of Rome.

Summary

The present thesis deals with the investigation of electrolyte and anode materials for IT-SOFCs, and in particular it is concerned with doped-ceria electrolytes and doped-$LaCrO_3$ anodes. New relationships between synthesis, structure, microstructure, catalytic and electrochemical properties have been found.

The study of heavily doped ceria has been treated following two different approaches: i. design of an effective combustion synthesis route for electrolyte materials and ii. elucidation of a possible correlation between structure and ionic conductivity.

In this light, firstly the effects of synthesis and sintering procedures on the electrochemical performance of $Ce_{0.8}Sm_{0.2}O_{2-x}$ have been taken into account. It has been demonstrated that it is possible to improve the total ionic conductivity of $Ce_{0.8}Sm_{0.2}O_{2-x}$ electrolyte by a careful choice of the SCS conditions and in particular that the combustion fuel directly shapes the microstructure and the grain boundary of the sintered powders. Grain boundary conductivity and total ionic conductivity are considerably improved by sucrose fuel, and this occurs also after sintering in reducing atmosphere.

Secondarily, it was evaluated a possible dependence of the ionic conductivity on short and long range structure. To this aim, the structural and electrical features of Sm, Er and Yb heavily doped ceria have been explored. The results obtained highlight the fundamental contribution of the grain boundary resistivity to the total resistance, which are mainly determined by the dopant nature as well as by the dopant concentration. The most striking result consists in the dependence of the ionic conductivity on cerium and dopant (Sm, Er, Yb) local structure. Samarium, remarkably known as one of the best dopants for ceria-based electrolytes, tends to behave differently from Er and Yb. XRD and EXAFS results point out more homogeneous distribution of Sm in the host lattice. Moreover, the evaluation of the first shell coordination number allows to discriminate a tendency of Sm to localize the oxygen vacancy mainly around cerium atoms and then to exclude a strong attractive interaction between the positively charged oxygen vacancies and the negatively charged trivalent cations.

As far as the anode material is concerned, $La_{0.9}Sr_{0.1}Cr_{0.7}Fe_{0.3}O_{3-\delta}$ has been identified as a promising anode material. Actually, it manifests more satisfying electrical and electrochemical features in reducing atmosphere with respect to the other materials taken into account in the present study. For a series of doped $LaCrO_3$ the role of iron and strontium doping has been clarified in details, giving a contribution to the basic knowledge on Cr-based perovskite-type materials as anode materials for IT-SOFCs fuelled with both hydrogen and methane. The evaluation of the electrical features of a series of MEAs points out the potentially good performance of the electrolyte-anode couple composed by $Ce_{0.8}Sm_{0.2}O_{2-x}$/ $La_{0.9}Sr_{0.1}Cr_{0.7}Fe_{0.3}O_{3-\delta}$.

References

[1] Steele, B.C.H.; Heinzel, A. *Nature* **2001**, 414, 345.

[2] Larminie, J.; Dicks, A. *Fuel Cell Systems Explained;* John Wiley & Sons, Ltd, England, **2003.**

[3] Jacobson, A.J. *Chem. Mater.* **2010**, 22, 660.

[4] Liu, M; Lynch, E.M.; Blinn, K.; Alamgir, F.M.; Choi, Y. *Mater. Today* **2011**, 14, 11, 534.

[5] Stambouli, A.B.; Traversa, E. *Renewable Sustainable Energy Rev.* **2002,** 6, 433.

[6] Tucker, M.C. *J. Power Sources* **2010**, 195, 4570.

[7] Goodenough, J.B. *Annu. Rev. Mater. Res.* **2003**, 33, 91.

[8] Inaba, H.; Tagawa, H. *Solid State Ionics* **1996**, 83, 1.

[9] Brett, D.J.L.; Atkinson, A.; Brandon, N.P.; Skinnerd, S.J. *Chem. Soc. Rev.* **2008**, 37, 1568.

[10] Aguadero, A.; Fawcett, L.; Taub, S.; Woolley, R.; Wu, K.T.; Xu, N.; Kilner, J.A.; Skinner, S.J. *J. Mater. Sci.* **2012**, 47, 3925.

[11] Sun, W. ; Zhu, Z.; Shi, Z.; Liu, W. *J. Power Sources* **2013**, 229, 95.

[12] Giannici, F.; Longo, A.; Deganello, F.; Balerna, A.; Arico, A.S.; Martorana, A. *Solid State Ionics* **2007**, 178, 587.

[13] Esposito, V.; Traversa, E. *J. Am. Ceram. Soc.* **2008**, 91, 1037.

[14] Wright, J.; Virkar, A.V. *J. Power Sources* **2011**, 196, 6118.

[15] Coll, D.P.; Núñez, P.; Frade, J.R. *J. Power Sources* **2013**, 227, 145.

[16] Cioatera, N.; Parvulescu, V.; Rolle, A.; Vannier, R.N. *Ceram. Int.* **2012**, 38, 5461.

[17] Bu, Y.F.; Zhong, Q.; Tan, W.Y.; Zhou, R.J.; Song, Y.; Cai, W. *Mater. Sci. Semicond. Process.* **2013**, 16, 2058.

[18] Hui, S.R.; Roller, J.; Yick, S.; Zhang, X.; Decès-Petit, C.; Xie, Y.; Maric, R.; Ghosh, D. *J. Power Sources* **2007**, 172, 493.

[19] Fu, Y.P.; Wen, S.B.; Lu, C.H. *J. Am. Ceram. Soc.* **2008**, 91, 127.

[20] Omata, T.; Goto, Y.; Matsuo, S.Y.M. *Sci. Technol. Adv. Mater.* **2007**, 8, 524.

[21] Dudek, M. *J. Eur. Ceram. Soc.* **2008**, 28, 965.

[22] Kahlaoui, M.; Inoubli, A.; Chefi, S.; Kouki, A.; Madani, A.; Chefi, C.; *Ceram. Int.* **2013**, 39, 6175.

[23] Chaubey, N.; Wani, B.N.; Bharadwaj, S.R.; Chattopadhyaya, M.C. *Solid State Sci*. **2013**, 20, 135.

[24] Yahiro, H.; Eguchi, K.; Arai, H. *Solid State Ionics* **1989**, 36, 71.

[25] Kharton, V.V.; Marques, F.M.B.; Atkinson, A. *Solid State Ionics* **2004**, 174, 135.

[26] McIntosh, S.; Gorte, R. J. *Chem. Rev.* **2004,** 104, 4845.

[27] Gorte, R.J.; Vohs, J.M. *Annu. Rev. Chem. Biomol. Eng.* **2011,** 2, 1.1.

[28] Hornés, A.; Gamarra, D.; Munuera, G.; Fuerte, A.; Valenzuela, R.X.; Escudero, M.J.; Daza, L.; Bera, P., Martinez-Arias, A. *J. Power Sources* **2009**, 192, 70.

[29] Hornès, A.; Gamarra, D.; Munuerab, G.; Conesa, J.C.; Martìnez-Arias, A. *J. Power Sources* **2007**, 169, 9.

[30] Toyir, J.; Gélin, P.; Belatel, H.; Kaddouri, A. *Catal. Today* **2010**, 157, 451.

[31] Zhu, W.Z.; Deevi, S.C. *Mater. Sci. Eng.* **2003**, A362, 228.

[32] Konysheva, E.; Irvine, J.T.S. *Chem. Mater.* **2009**, 21, 1514.

[33] Oishi, M.; Yashiro, K.; Sato, K.; Mizusaki, J.; Kawada, T. *J. Solid State Chem.* **2008**, 181, 3177.

[34] Papazisi, K.M.; Balomenou, S.; Tsiplakides, D. *J. Appl. Electrochem.* **2010**, 40, 1875.

[35] Setz, L.F.G.; Santacruz, I.; Colomer, M.T.; Mello-Castanho, S.R.H.; Moreno, R.; *Mater. Res. Bull.* **2011**, 46, 983.

[36] Bhatt, H.; Bahadur, J.; Deo, M.N.; Ramanathan, S.; Pandey, K.K.; Sen, D.; Mazumder, S.; Sharma, S.M. *J. Solid State Chem.***2011**, 184, 204.

[37] Prabhakaran, K.; Lakra, J.; Beigh, M.O.; Gokhale, N.M.; Sharma, S.C.; Lal, R. *J. Mater. Sci.* **2005**, 41, 6300.

[38] Lee, G.Y.; Song, R.H.; Kim, J.H.; Peck, D.H.; Lim, T.H.; Shul, Y.G.; Shin, D.R. *J. Electroceram.* **2006**, 17, 723.

[39] Mukherjee, S.; Gonal, M.R.; Patel, M.K.; Roy, M.; Patra, A.; Tyagi, A.K. *J. Am. Ceram Soc.* **2011**, 1, 6.

[40] Fu, Y.P.; Wang, H.C.; Hu, S.H.; Tay, K.W. *Ceram. Int.* **2011**, 37, 2127.

[41] Kolotygin, V.A.; Tsipis, E.V.; Lü, M.F.; Pivak, Y.V.; Yarmolenko, S.N.; Bredikhin, S.N.; Kharton, V.V. *Solid State Ionics* **2013**, 251, 28.

[42] Tao, S.; Irvine, J.T.S. *Chem. Mater.* **2004**, 16, 4116.

[43] Danilovic, N.; Vincent, A.; Luo, J.L.; Chuang, K.T.; Hui, R; Sanger, A.R. *Chem. Mater.* **2010**, 22, 957.

[44] Lay, E.; Benamira, M.; Pirovano, C.; Gauthier, G.; Dessemond, L. *Fuel Cells* **2012**, 12, 265.

[45] Van den Bossche, M.; McIntosh, S. *J. Catal.* **2008**, 255, 313.

[46] Vert, V.B.; Melo, F.V., Navarrete, L., Serra, J.M. *Appl. Catal., B* **2012**, 115, 346.

[47] McIntosh, S.; van den Bossche, M. *Solid State Ionics* **2011**, 192, 453.

[48] Tao, S.; Irvine, J.T.S. *J. Electrochem. Soc.* **2004**, 151, A252.

[49] Tao, S.; Irvine, J.T.S. *Chem. Mater.* **2006**, 18, 5453.

[50] Dong, X.; Ma, S; Huang, K.; Chen, F. *Int. J. Hydrogen Energy* **2012**, 37, 10866.

[51] Sfeir, J. *J. Power Sources* **2003**, 118, 276.

[52] Sfeir, J.; Buffat, P.A.; Mockli, P.; Xanthopoulos, N.; Vasquez, R.; Mathieu, H.J.; Van herle, J. Ravindranathan Thampi, K. *J. Catal.* **2001**, 202, 229.

[53] Lü, M.F.; Tsipis, E.V.; Waerenborgh, J.C.; Yaremchenko, A.A.; Kolotygin, V.A.; Bredikhin, S.; Kharton, V.V. *J. Power Sources* **2012**, 206, 59.

[54] Jiang, S.P.; Chan, S.H. *J. Mater. Sci.* **2004**, 39, 4405.

[55] Zhu, X.; Zhong, Q.; Zhao, X.; Yan, H. *Appl. Surf. Sci.* **2011**, 257, 1967.

[56] Van den Bossche, M.; McIntosh, S. *Chem. Mater* .**2010**, 22, 5856.

[57] Deleebeeck, L.; Fournier, J.L.; Birss, V. *Solid State Ionics* **2010**, 181, 1229.

[58] Sun, C.; Li, H.; Chen, L. *Energy Environ. Sci.* **2012**, 5, 8475.

[59] Trovarelli, A. *Catalysis Reviews: Sci. Eng.***1996**, 38, 439.

[60] Liotta, L.F.; Macaluso , A.; Longo, A.; Pantaleo, G.; Martorana, A.; Deganello, G. *Appl. Catal., A* **2003**, 240, 295.

[61] Deganello, F.; Martorana, A. *J. Solid State Chem.* **2002**, 163, 527.

[62] Martorana, A.; Deganello, G.; A. Longo, A.; Prestianni, A.; Liotta, L.; Macaluso, A.; Pantaleo, G.; Balerna, A.; Mobilio, S. *J. Solid State Chem.* **2004**, 177, 1268.

[63] Deganello, F.; Longo, A.; Martorana, A. *J. Solid State Chem.* **2003**, 175, 289.

[64] Mogensen, M.; Sammes, N.M.; Tompsett, G.A. *Solid State Ionics* **2000**, 129, 63.

[65] Steele, B.C.H. *Solid State Ionics* **2000**, 129, 95.

[66] Xiong, Y.P.; Kishimoto, H.; Yamaji, K.; Yoshinaga, M.; Horita, T.; Brito, M.E.; Yokokawa, H. *Solid State Ionics* **2011**, 192, 476.

[67] Kim, S.; Maier, J. *J. Electrochem. Soc.* **2002**, 149, J73.

[68] Lupetin, P.; Giannici, F.; Gregori, G.; Martorana, A.; Maier, J. *J. Electrochem. Soc.***2012**, 159, B417.

[69] Vegard, L. *Zeitschrift für Physik* **1921,** 5, 17.

[70] Vegard, L. *Zeitschrift für Kristallographie* **1928**, 67, 239.

[71] Kim, D.J. *J. Am. Ceram. Soc.* **1989**, 72, 1415.

[72] Tschöpe, A.; Sommer, E.; Birringer, R. *Solid State Ionics* **2001**, 139, 255.

[73] Tschöpe, A. *Solid State Ionics* **2001**, 139, 267.

[74] Tschöpe, A.; Kilassonia, S.; Birringer, R. *Solid State Ionics* **2004**, 173, 57.

[75] Maier, J. *Prog. Solid State Chem.* **1995**, 23, 171.

[76] Maier, J. *Berichte der Bunsengesellschaft für physikalische Chemie* **1986,** 90, 26.

[77] Maier, J. *Physical Chemistry of Ionic Materials;* John Wiley & Sons, Ltd, England, 2004.

[78] Maier, J. *Solid State Ionics* **2002**, 148, 367.

[79] Hwang, J.H.; Mclachlan, D.S.; Mason, T.O. *J. Electroceram.* **1999**, 3, 7.

[80] Lupetin, P. Charge carrier defect chemistry of nanoscopic $SrTiO_3$, Ph.D. Thesis, *The University of Stuttgart,* March 2012.

[81] Göbel, M.C.; Gregori, G.; Guo, X.X.; Maier, J. *Phys. Chem. Chem. Phys.* **2010**, 12, 14351.

[82] Lee, H.B.; Prinz, F.B.; Cai, W. *Acta Mater.* **2013**, 61, 3872.

[83] Tanaka, R.; Oliveira, W.S. ; Brandão, A.; Abrantes, J.C.C.; Frade, J.R. *Electrochim. Acta* **2012**, 85, 116.

[84] Lee, J.H. *Monatsh Chem* **2009**, 140, 1081.

[85] Guo, X.; Zhang, Z. *Acta Mater.* **2003**, 51, 2539.

[86] Esposito, V.; Ni, D.W.; He, Z.; Zhang, W.; Prasad, A.S.; Glasscock, J.A.; Chatzichristodoulou, C.; Ramousse, S.; Kaiser, A. *Acta Mater.* **2013**, 61, 6290.

[87] Anantharaman, S.B.; Baurin, R. *Ceram. Int.* **2013**, 39, 9421.

[88] Badwal, S.P.S.; Fini, D.; Ciacchi, F.T.; Munnings, C.; Kimpton, J.A.; Drennan, J. *J. Mater. Chem. A* **2013**, 1, 10768.

[89] Ayawanna, J.; Wattanasiriwech, D.; Wattanasiriwech, S.; Aungkavattana, P. *Solid State Ionics* **2009**, 180, 1388.

[90] Balaguer, M.; Solís, .; Serra, J.M. *J. Phys. Chem. C* **2012**, 116, 7975.

[91] Panigrahi, S.; Biswal, R.C.; Anwar, S.; Besra, L.; Bhattacharjee, S. *J. Am. Ceram. Soc.* **2013**, 96, 2846.

[92] Lapa, C.M.; Figueiredo, F.M.L.R.; Marques, F.M.B.; de Souza, D.P.F. *Solid State Ionics* **2012**, 225, 424.

[93] Khakpour, Z.; Yuzbashi, A.; Maghsodipour, A.; Ahmadi, K.; *Solid State Ionics* **2012**, 227, 80.

[94] Mori, T.; Drennan, J. *J. Electroceram.* **2006**, 17, 749.

[95] Acharya, S.A. *J. Power Sources* **2012**, 198, 105.

[96] Esposito, V.; Zunic, M.; Traversa, E.; *Solid State Ionics* **2009**, 180 1069.

[97] Zheng, Y.; Zhou, M.; Ge, L.; Li, S.; Chen, H.; Guo, L. *J. Alloys Compd.* **2011**, 509, 1244.

[98] Kim, G.; Lee, N.; Kim, K.B.; Kim, B.K.; Chang, H.; Song, S.J.; Park, J.Y. *Int. J. Hydrogen Energy* **2013**, 38, 1571.

[99] Jaiswal, N.; Kumar, D.; Upadhyay, S.; Parkash, O. *J. Alloys Compd.* **2013**, 577, 456.

[100] Pikalova, E.Y.; Murashkina, A.A.; Maragou, V.I.; Demin, A.K.; Strekalovsky, V.N.; Tsiakaras, P.E. *Int. J. Hydrogen Energy* **2011**, 36, 6175.

[101] Sánchez-Bravo, G.B.; García, O.; Gálvez-Sánchez, M.; Violero, J.M.; Rosa, A.; Carpena, I.; Ruiz-Morales, J.C.; Canales-Vázquez, J. *J. Eur. Ceram. Soc.* **2013**, 33, 1825.

[102] Jang, C.H.; Jung, D.S.; Kim, J.H.; Kang, Y.C.; Cho, Y.H.; Lee, J.H. *Ceram. Int.* **2010**, 36, 465.

[103] Anselmi-Tamburini, U.; Maglia, F.; Chiodelli, G.; Tacca, A.; Spinolo, G.; Riello, P.; Bucella, S.; Munir, Z.A. *Adv. Funct. Mater.* **2006,** 16, 2363.

[104] Bucevac, D.; Radojkovic, A.; Miljkovic, M.; Babic, B.; Matovic, B. *Ceram. Int.* **2013**, 39, 3603.

[105] Deganello, F.; Esposito, V.; Miyayama, M.; Traversa, E. *J. Electrochem. Soc.* **2007,** 154, A89.

[106] Deganello, F.; Marcì, G.; Deganello, G. *J. Eur. Ceram. Soc.* **2009**, 29, 439.

[107] Deganello, F.; Liotta, L.F.; Marcì, G.; Fabbri, E.; Traversa, E. *Mater. Renewable Sustainable Energy* **2013**, 2, 8.

[108] Mangalaraja, R.V.; Ananthakumar, S.; Schachtsiek, A.; López, M. Camurri, C.P.; Avila, R.E. *Mater. Sci. Eng. A* **2010**, 527, 3645.

[109] Dong, Y.; Hampshire, S.; Zhou, J.; Dong, X.; Lin, B.; Meng, G.; *J. Eur. Ceram. Soc.* **2011**, 31, 2365.

[110] Singh, N.K.; Singh, P.; Singh, M.K.; Kumar, D.; Parkash, O. *Solid State Ionics* **2011**, 192, 431.

[111] Mahata, T.; Das, G.; Mishra, R.K.; Sharma, B.P. *J. Alloys Compd.* **2005**, 391,129.

[112] Wu, W.C.; Huang, J.T.; Chiba, A. *J. Power Sources* **2010**, 195, 5868.

[113] Mokkelbost, T.; Kaus, I.; Grande, T.; Einarsrud, M.A. *Chem. Mater.* **2004**, 16, 5489.

[114] Skalar, T.; Macek, J.; Golobic, A. *J. Eur. Ceram. Soc.* **2012**, 32, 2333.

[115] Tian, R.; Zhao, F.; Chen, F.; Xia, C. *Solid State Ionics* **2011**, 192, 580.

[116] Fu, Y.P.; Lin, C.H.; Liu, C.W.; Tay, K.W.; Wen, S.B. *J. Power Sources* **2006**, 159, 38.

[117] Dong, Y.; Li, D.; Feng, X.; Dong, X.; Hampshire, S. *RSC Adv.* **2013**, 3, 17395.

[118] Chavan, S.V.; Sastry, P.U.; Tyagi, A.K. *J. Alloys Compd.* **2008**, 457, 440.

[119] Lenka, R.K.; Mahata, T.; Sinha, P.K.; Sharma, P. *J. Am. Ceram. Soc.* **2006**, 89, 3871.

[120] Lenka, R.K.; Mahata, T.; Tyagi, A.K.; Sinha, P.K. *Solid State Ionics* **2010,** 181, 262.

[121] Kosinski, M.R.; Baker, R.T. *J. Power Sources* **2011,** 196, 2498.

[122] Shigapov, A.N.; Graham, G.W.; McCabeb, R.W.; Plummer H.K. *J. Appl. Catal. A: General* **2001**, 210, 287.

[123] Zhou, W.; Shao, Z.P.; Ran, R.; Jin, W.Q.; Xu, N.P. *Mater. Res. Bull.* **2008,** 43, 2248.

[124] Ma, J.; Jiang, C.; Zhou, X.; Meng, G.; Liu, X. *J. Alloys Compd.* **2008**, 455, 364.

[125] Ianos, R.; Taculescu, A.; Pacurariu, C.; Lazau, I. *J. Am. Ceram. Soc.* **2012,** 95, 2236.

[126] Das, R.N. *Mater. Lett.* **2001,** 47, 344.

[127] Biswas, M. *J. Alloys Compd.* **2009**, 480, 942.

[128] Bose, S.; Wu, Y. *J. Am. Ceram. Soc.* **2005,** 88, 1999.

[129] Jain, S.R.; Adiga, K.C.; Verneker, V.R.P. *Combust. Flame***1981**, 40, 71.

[130] Da Silva, A.L.A; Castro, G.G.G.; Souza M.M.V.M *J. Therm. Anal. Calorim.* **2012**, 109, 33.

[131] Souza, E.C.C. *J. Electroceram.* **2013**, 31, 245.

[132] Chueh, W.C.; McDaniel, A.H.; Grass, M.E.; Hao, Y.; Jabeen, N.; Liu, Z.; Haile, S.M.; McCarty, K.F.; Bluhm, H.; El Gabaly, F. *Chem. Mater.* **2012**, 24, 1876.

[133] Wang, H.; Chroneos, A.; Schwingenschlögl, U. *J. Chem. Phys.* **2013**, 138, 224705.

[134] Hooper, J.; Ismail, A.; Giorgi, J.B.; Woo, T.K. *Phys. Chem. Chem. Phys.* **2010**, 12, 12969.

[135] Ismail, A.; Hooper, J.; Giorgi, J.B.; Woo, T.K. *Phys. Chem. Chem. Phys.* **2011**, 13, 6116.

[136] Ismail, A.; Giorgi, J.B.; Woo, T.K. *J. Phys. Chem. C* **2012**, 116, 704.

[137] Farra,R. García-Melchor, M.; Eichelbaum, M.; Hashagen, M.; Frandsen, W.; Allan, J.; Girgsdies, F.; Szentmiklósi, L.; López, N.; Teschner, D. *Catal.* **2013**, 3, 2256.

[138] Huang, C.W.; Wei, W.C.J.; Chen, C.S.; Chen, J.C. *J. Eur. Ceram. Soc.* **2011**, 31, 3159.

[139] Nakayama, M.; Ohshima, H.; Nogami, M.; Martin, M. *Phys. Chem. Chem. Phys.* **2012**, 14, 6079.

[140] Paier, J.; Penschke, C; Sauer, J. *Chem. Rev.* **2013**, 113, 3949.

[141] Dholabhai, P.P.; Adams, J.B. *J. Mater. Sci.* **2012**, 47, 7530.

[142] Shannon, R.D. *Acta Crystallogr.* **1969**, B25, 925.

[143] Ohashi, T.; Yamazaki, S.; Tokunaga, T.; Arita, Y.; Matsui, T.; Harami, T.; Kobayashi, K. *Solid State Ionics* **1998**, 113–115, 559.

[144] Nitani, H.; Nakagawa, T.; Yamanouchi, M.; Osuki, T.; Yuya, M.; Yamamoto, T.A. *Mater. Lett.* **2004**, 58, 2076.

[145] Ou, D.R.; Mori, T.; Ye, F.; Zou, J.; Auchterlonie, G.; Drennan, *J. Phys. Rev. B* **2008**, 77, 024108.

[146] Yamazaki, S.; Matsui, T.; Ohashi, T.; Arita, Y. *Solid State Ionics* **2000**, 136, 913.

[147] Ohashi, T; Yamazaki, S.; Tokunaga, T.; Arita, Y.; Matsui, T.; Harami, T.; Kobayashi, K. **1998**, 113, 559.

[148] Chadwick, A.V.; Savin, S.L.P. *J. Alloys Compd.* **2009**, 488, 1.

[149] Ahn, K.; Yoo, D.S.; Prasad, D.H.; Lee, H.W.; Chung, Y.C.; Lee, J.H. *Chem. Mater.* **2012,** 24, 4261.

[150] Yashima, M.; Nobuo, I.; Yoshimura, M.; *J. Am. Ceramic. Soc.* **1992**, 75, 1541.

[151] Spanier, J.E.; Robinson, R.D.; Zhang, F.; Chan, S.W.; Herman, I P. *Phys. Rev. B* **2001**, 64, 245407.

[152] Guo, M.; Lu, J.; Wu, Y.; Wang, Y.; Luo, M. *Langmuir* **2011**, 27, 3872.

[153] Kosacki, I.; Suzuki, T.; Anderson, H.U.; Colomban, P. *Solid State Ionics* **2002**, 149, 99.

[154] Kosacki, I.; Petrovsky, V.; Anderson, H.U. *J. Am. Ceram Soc.* **2002**, 85, 2646.

[155] Ahamed, S.Z.A.; Reddy, C.M.; Raju, B.D.P. *Spectrochim. Acta, Part A* **2013**, 103, 246.

[156] Shen, Y.; Chambers, M.D.; Clarke, D.R. *Surf. Coat. Technol.* **2008**, 203, 456.

[157] Sakirzanovas, S.; Katelnikovas, A.; Bettentrup, H.; Kareiva, A.; Justel, T. *J. Lumin.* **2011**, 131, 1525.

[158] Tiseanu, C.; Cojocaru, B.; Avram, D.; Parvulescu, V. I.; Vela-Gonzalez, A.V.; Sanchez-Dominguez, M. *J. Phys. D: Appl. Phys.* **2013**, 46, 275302.

[159] Maglia, F.; Farina, F.; Dapiaggi, M.; Tredici, I.G.; Anselmi-Tamburini, U. *Solid State Ionics* **2012**, 225, 412.

[160] Souza, E.C.C.; Chueh, W.C.; Jung, W.; Muccillo, E. N. S.; Haile, S.M. *J. Electrochem. Soc.* **2012**, 159, K127.

[161] Avila-Paredes, H.J.; Choi, K.; Chen, C.T.; Kim, S. *J. Mater. Chem.* **2009**, 19, 4837.

[162] Primdahl, S.; Hansen, J.R.; Grahl-Madsen, L.; Larsen, P.H. *J. Electrochem. Soc.* **2001**, 148, A74.

[163] Zha, S.; Tsang, P.; Cheng, Z.; Liu, M. J. *Solid State Chem.* **2005**, 178, 1844.

[164] Bruce, M.K.; van den Bossche, M.; McIntosh, S. *J. Electrochem. Soc.* **2008**, 155, B1202.

[165] Van den Bossche, M.; Matthews, R.; Lichtenberger, A.; McIntosh, S. *J. Electrochem. Soc.* **2010**, 157, B392.

[166] Tezuka, K.; Hinatsu, Y.; Nakamura, A.; Inami, T.; Shimojo, Y.; Morii, Y. *J. Solid State Chem.* **1998**, 141, 404.

[167] Oikawa, K.; Kamiyama, T.; Hashimoto, T.; Shimojyo, Y.; Morii, Y. *J. Solid State Chem.* **2000,** 154, 524.

[168] Chakraborty, K.R.; Yusuf, S.M.; Krishna, P.S.R.; Ramanadham, M.; Tyagi M.; Pomjakushin, V. *J. Phys.: Condens. Matter* **2006**, 18 8661.

[169] Peña, M.A.; Fierro, J.L.G. *Chem. Rev.* **2001**, 101, 1981.

[170] Lufaso, M.W. Perovskite synthesis and analysis using structure prediction diagnostic software, Ph.D. Thesis, *The University of Ohio State*, 2002.

[171] Mizusaki, J.; Yamauchi, S.; Fueki, K.; Ishikawa, A. *Solid State Ionics* **1984**, 12, 119.

[172] Anderson, H.U. *Solid State Ionics* **1992**, 52, 33.

[173] Plint, S.M.; Connor, P.A.; Tao, S.; Irvine, J.T.S. *Solid State Ionics* **2006**, 177, 2005.

[174] Mizusaki, J. *Solid State Ionics* **1992**, 52, 79.

[175] Mizusaki, J.; Sasamoto, T.; Cannon, W.R.; Bowen, H.K. *J. Am. Ceram. Soc.* **1983**, 66, 247.

[176] Mizusaki, J.; Sasamoto, T.; Cannon, W.R.; Bowen, H.K. *J. Am. Ceram. Soc.* **1982**, 65, 363.

[177] Van Roosmalen, J.A.M.; Huijsmans, J.P.P., Plomp, L. *Solid State Ionics* **1993**, 66, 279.

[178] Thomas, E.; Lee, H.D.; Yoon, M.Y.; Ehrman, S.H.; Hwang, J.H. *Ceram. Int.* **2011**, 37, 2269.

[179] Channu, V.S.R.; holze, R.; Walker, E.H., Kalluru, R.R. *New J. Glass Ceram.* **2011**, 1, 58.

[180] Rashad, M.M.; El-Sheikh, S.M. *Mater. Res. Bull.* **2011**, 46, 469.

[181] Setz, L.F.G.; Mello-Castanho, S.R.H.; Moreno, R.; Colomer, M.T. *Int. J. Appl. Ceram. Technol.* **2009**, 6, 626.

[182] Tao, S.; Irvine, J.T.S. *Solid State Ionics* **2008**, 179, 725.

[183] Tan, W.; Zhong, Q.; Xu, D.; Yan, H.; Zhu, X. *Int. J. Hydrogen Energy* **2013**, 38, 16656.

[184] Khine, M.S.S.; Chen, L., Zhang, S.; Lin, J.; Jiang, S.P. *Int. J. Hydrogen Energy* **2013**, 38, 13300.

[185] Mihai, O.; Chen, D.; Holmen, A.; *J. Catal.* **2012**, 293, 175.

[186] Specchia, S.; Galletti, C.; Specchia, V. *Stud. Surf. Sci. Catal.* **2010**, 175, 59.

[187] Liotta, L.F.; Macaluso, A.; Pantaleo, G.; Longo, A.; Marcì, G.; Gialanella, S. *J. Sol-Gel Sci. Technol.* **2003**, 26, 235.

[188] Pechini, M., US Patent, 3,330,697, 1967.

[189] Hernandez, T.; Bautista, M. C. *J. Eur. Ceram. Soc.* **2005**, 25, 663.

[190] Larson, A.C.; Von Dreele, R.B.: GSAS general structure analysis system. LANSCE, MS-H 805, Los Alamos National Laboratory, Los Alamos, NM 87545, USA (1998).

[191] Toby, B.H. *J. Appl. Crystallogr.* **2001**, 34, 210.

[192] Toby, B.H. *Powder Diffr.* **2006**, 21, 67.

[193] McCusker, L.B.; Von Dreele, R.B.; Coxd, D.E.; Louer, D.; Scardi, P. *J. Appl. Cryst.* **1999**, 32, 36.

[194] Klementev, K.V. *J. Phys. D: Appl. Phys.* **2001**, 34, 209.

[195] Ankudinov, A.L.; Ravel, B.; Rehr, J.J.; Conradson, S.D. *Phys. Rev. B* **1998**, 58, 7565.

[196] Brunauer, S.; Emmett, P.H.; Teller, E *J. Am. Chem. Soc.* **1938**, 60, 309.

[197] Van der Pauw, L.J. *Philips Res. Repts* **1958**, 13, 1.

Acknowledgments

I thank Professor Antonino Martorana, Dr. Francesca Deganello, Dr. F. Giannici, Dr. F.L. Liotta and Dr. Giuliano Gregori for their constant encouragement and support as well as the numerous opportunities offered to me over the years. I am grateful to Dr. Alessandro Longo, Dr. Anna Maria Venezia, the scientific group of CNR-ISMN of Palermo, Dr. Franco Padella, Dr. Claudia Paoletti, Dr. Elisabetta Simonetti, the scientific group of ENEA-UTTMAT-CHI Casaccia of Rome and Professor Reginaldo Muccillo for their precious contribution to this thesis. I am sincerely thankful to Professor Joachim Maier and all his department of Max Planck Institute for Solid State Research of Stuttgart for having given me the opportunity to live a fantastic professional and human experience.

Curriculum vitae

Name	Chiara Aliotta
Date of birth	14/10/1983
Place of birth	Palermo, Italy

Full career

- 2011- 2013 - Ph.D student in Chemical Sciences at the University of Palermo in partnership with National Reaserch Center.
  Title: "*Study of advanced materials for solid oxide fuel cells: influence of dopants and synthesis procedures on anode and electrolyte properties.*"

- 11/09/2012 -19/12/2012 - visiting student of the department of Professor Joachim Maier under supervision of Dr. Giuliano Gregori at the Max Planck Institute of Stuttgart, Germany.

- 02/04/2013 - 30/04/2013 - visiting student of the department of Professor Joachim Maier under supervision of Dr. Giuliano Gregori at the Max Planck Institute for Solid State Research of Stuttgart, Germany.

- 2009 - Qualification exam for the Italian board of chemists.

- 2006-2009 - Master School in Chemistry at the University of Palermo, Italy, in partnership with ENEA-CASACCIA research institute of Rome, Italy . Title of the final thesis: "*Mechanochemical synthesis of magnetic nanoparticles and development of ferrofluids in aqueous solutions* ".

- 2007-2008 - Specialization school on *"Expert in nanotechnology for Cultural Heritage"* at the University of Palermo, Italy.

- 31/12/2008 - 31/03/2009 - Postgraduate fellowship FiXo University of Palermo and ENEA-CASACCIA research institute of Rome, Italy.

- 2002-2005 - Bachelor School in Chemistry at the University of Palermo, Italy. Title of the final thesis: "*Application of neutron techniques on geologic materials*".

Scientific publication

- M. Bellusci, C. Aliotta, D. Fiorani, A. La Barbera, F. Padella, D. Peddis, M. Pilloni, D. Secci Manganese Iron Oxide Superparamagnetic Powder by Mechanochemical Processing. Nanoparticles Functionalization and Dispersion in a Nanofluid, Journal of Nanoparticle Reaserch, 2012, 14:904.

- F.Giannici, C.Aliotta, G.Gregori, A.Longo, J.Maier, A.Martorana Heavily-doped cerium oxide: defect association and oxygen-ion conductivity, manuscript in preparation.

- C.Aliotta, F.Deganello, E.N.S. Muccillo, R.Muccillo, A. Martorana New synthetic strategies for the enhancement of the ionic conductivity in $Ce_{0.8}Sm_{0.2}O_{2-x}$, manuscript in preparation.

- C.Aliotta, F.Deganello, L.F.Liotta, C.Paoletti, A.Martorana Structural, catalytic and electrical investigation on $La_{1-x}Sr_xCr_{1-y}Fe_yO_{3-\delta}$ as anodes for IT-SOFCs, manuscript in preparation.

Oral presentation

- C.Aliotta, F.Deganello, E.N.S. Muccillo, R.Muccillo *New synthetic strategies for the enhancement of the ionic conductivity in* $Ce_{0.8}Sm_{0.2}O_{2-x}$*",* 6th International Conference on Electroceramics, 09-13 November, João Pessoa, Brazil.

- C.Aliotta, F.Deganello, L.F.Liotta, C.Paoletti, A.Martorana *"From Interconnectors to anode materials for IT-SOFCS: the role of iron in* $La_{1-y}Sr_yCr_{1-x}Fe_xO_{3-\delta}$*",* XVII National Congress of Catalysis 2013 and XI National Congress of Zeolites Science and Techonology, 15-18 September, Riccione, Italy.

- M.Bellusci, C.Aliotta, A.La Barbera, G.Ennas, D.Fiorani, F.Padella, D.Peddis, F.Varsano, *Synthesis of manganese iron oxide nanoparticles from metal salts* *by High Energy Ball Milling*", IX National Meeting Nanophase Materials, 3-5 June 2009, Cagliari, Italy.

Poster

- C.Aliotta, F.Deganello, L.F.Liotta, A.Martorana *Structural, catalytic and electrical investigation on* $La_{1-x}Sr_xCr_{1-y}Fe_yO_{3-\delta}$ *as anodes for IT-SOFCs,* 8th International Conference on f-elements, 26-31 August 2012, Udine, Italy.

- M.Bellusci, C.Aliotta, A.La Barbera, G.Ennas, D.Fiorani, F.Padella, D.Peddis F.Varsano *Manganese Iron Oxide Ferrofluids by Mechanochemical Approach,* NANOTECHITALY2010, 20-22 October 2010, Venice, Italy.

Scientific activity

- 16-27/09/2013 - XII School of Synchrotron light, Grado, Italy.

- 15-18/09/2013 - XVII National Congress of Catalysis 2013 and XI National Congress of Zeolites Science and Techonology, , Riccione, Italy.

- 28-3/07/2013 - EXAFS measurements (n.° 20130072) at the Elettra-Synchrotron, Trieste, Italy.

- 26-31/08/2012 - 8th International Conference on f-elements, , Udine, Italy.

- 27/09/2011-04/10/2011 - EXAFS measurements (n.° MA-1223) at the ESRF-Synchrotron, Grenoble, France.

- 4-7/04/2011 - EXAFS measurements (n.° 20105447) at the Elettra-Synchrotron, Trieste, Italy.